

Revision 1

High Concentrations of Manganese and Sulfur in Deposits on Murray Ridge, Endeavour Crater, Mars

Raymond E. Arvidson¹, Steven W. Squyres², Richard V. Morris³, Andrew H. Knoll⁴, Ralf Gellert⁵,
Benton C. Clark⁶, Jeffrey G. Catalano¹, Brad L. Jolliff¹, Scott M. McLennan⁷, Kenneth E.
Herkenhoff⁸, Scott VanBommel⁵, David W. Mittlefehldt³, John P. Grotzinger⁹, Edward A.
Guinness¹, Jeffrey R. Johnson¹⁰, James F. Bell III¹¹, William H. Farrand⁶, Nathan Stein¹, Valerie
K. Fox¹, Matthew P. Golombek¹², Margaret A. G. Hinkle¹, Wendy M. Calvin¹³ and Paulo A. de
Souza Jr.¹⁴

¹Dept. of Earth and Planetary Sciences, Washington University in Saint Louis, St. Louis, MO 63130, U.S.A.

²Dept. of Astronomy, Cornell University, Ithaca, NY 14853, U.S.A.

³Johnson Space Center, Houston, TX 77058, U.S.A.

⁴Department of Organismic and Evolutionary Biology, Harvard University, Cambridge, MA 02138, U.S.A.

⁵Dept. of Physics, University of Guelph, Guelph, ON N1G 2W1, Canada

⁶Space Science Institute, Boulder, CO 80301, U.S.A.

⁷Department of Geosciences, Stony Brook University, Stony Brook, NY 11794, U.S.A.

⁸U.S. Geological Survey, Astrogeology Science Center, Flagstaff, AZ 86001, U.S.A.

⁹Division of Geological and Planetary Sciences, California Institute of Technology, Pasadena, CA 91125, U.S.A.

¹⁰Johns Hopkins University, Applied Physics Laboratory, Laurel, MD 20723, U.S.A.

¹¹School of Earth & Space Exploration, Arizona State University, Tempe, AZ 85281, U.S.A.

¹²California Institute of Technology/Jet Propulsion Laboratory

Pasadena, CA 91011

¹³Geological Sciences and Engineering, University of Nevada, Reno, NV 89503, U.S.A.

¹⁴CSIRO Digital Productivity Flagship, Hobart, TAS 7004, Australia

To be submitted to *American Mineralogist*

Draft: 10/19/15

Revised 1/20/16

17 **Abstract**

18 Mars Reconnaissance Orbiter HiRISE images and Opportunity rover observations of the
19 ~22 km wide Noachian age Endeavour Crater on Mars show that the rim and surrounding terrains
20 were densely fractured during the impact crater-forming event. Fractures have also propagated
21 upward into the overlying Burns formation sandstones. Opportunity's observations show that the
22 western crater rim segment, called Murray Ridge, is composed of impact breccias with basaltic
23 compositions, as well as occasional fracture-filling calcium sulfate veins. Cook Haven, a gentle
24 depression on Murray Ridge, and the site where Opportunity spent its sixth winter, exposes highly
25 fractured, recessive outcrops that have relatively high concentrations of S and Cl, consistent with
26 modest aqueous alteration. Opportunity's rover wheels serendipitously excavated and overturned
27 several small rocks from a Cook Haven fracture zone. Extensive measurement campaigns were
28 conducted on two of them: Pinnacle Island and Stuart Island. These rocks have the highest
29 concentrations of Mn and S measured to date by Opportunity and occur as a relatively bright
30 sulfate-rich coating on basaltic rock, capped by a thin deposit of one or more dark Mn oxide
31 phases intermixed with sulfate minerals. We infer from these unique Pinnacle Island and Stuart
32 Island rock measurements that subsurface precipitation of sulfate-dominated coatings was
33 followed by an interval of partial dissolution and reaction with one or more strong oxidants (e.g.,
34 O₂) to produce the Mn oxide mineral(s) intermixed with sulfate-rich salts coating phases. In
35 contrast to arid regions on Earth, where Mn oxides are widely incorporated into coatings on
36 surface rocks, our results demonstrate that on Mars the most likely place to deposit and preserve
37 Mn oxides was in fracture zones where migrating fluids intersected surface oxidants, forming
38 precipitates shielded from subsequent physical erosion.

39 **Keywords:** Mars, geochemistry, mineralogy, manganese oxides, sulfates

40

41

Introduction

42 Recent observations by the Opportunity Mars rover on the Cape York rim segment of the
43 Noachian-age 22 km wide Endeavour Crater (Fig. 1) revealed evidence for aqueous mobilization
44 of Zn and precipitation of gypsum in veins (Squyres et al. 2012), together with the formation of
45 phyllosilicate minerals in and along fractures (Arvidson et al. 2014). In parallel, the Curiosity
46 rover in Gale Crater has uncovered morphologic, compositional, and mineralogic evidence for a
47 broadly coeval fluvial-deltaic-lacustrine system and associated diagenetic alteration of
48 sedimentary rocks of basaltic composition (Grotzinger et al. 2014, 2015). These discoveries add
49 to the growing evidence from orbital and landed missions that early Mars supported extensive
50 water-related alteration of crustal materials in both surface and subsurface environments (e.g.,
51 Poulet et al. 2005; Ehlmann and Edwards 2014). In this paper we describe Opportunity
52 measurements acquired while exploring the Murray Ridge rim segment of Endeavour Crater (Figs.
53 2-4, Table 1). We first provide an overview of Opportunity's traverses and measurements on
54 Murray Ridge and consider the implications for past aqueous processes based on exposed bedrock
55 measurements. We then focus on rocks named Pinnacle Island and Stuart Island that were
56 serendipitously excavated from a fracture by Opportunity's wheels. These rocks have unique
57 coatings with the highest Mn and S concentrations found thus far at Meridiani Planum. The data
58 imply aqueous precipitation of sulfate-rich salts, followed by introduction of a strong oxidant that
59 led to precipitation of one or more Mn oxide(s).

60

Opportunity Rover and Instrument Payload

61 Opportunity is a six-wheeled, solar-powered rover (Squyres et al. 2003) equipped with
62 mast-based Pancam multispectral stereo cameras with 13 filters covering the 0.432 to 1.05 μm
63 spectral region (Bell et al. 2003), a robotic arm (instrument deployment device or IDD) with a

64 Microscopic Imager (MI) that can acquire panchromatic images with 31 μm pixel sizes
65 (Herkenhoff et al. 2003), an Alpha Particle X-ray Spectrometer (APXS) to determine the target
66 chemical compositions (Gellert et al. 2006), and a Rock Abrasion Tool (RAT) to brush loose dust
67 and sand from targets and/or to grind into rocks to remove indurated coatings or weathering rinds
68 (Gorevan et al. 2003). In addition, the rover carries mast-mounted stereo cameras for navigation
69 and terrain context measurements (Navcams), and front and rear body-mounted stereo cameras
70 (Hazcams) used for hazard avoidance during traverses and fine-scale placement of IDD-based
71 instruments onto rock and soil targets. The science instrument payload also includes the Mini-
72 TES thermal emission spectrometer and a Mössbauer Spectrometer, but these two instruments
73 were no longer functioning during the time period covered by this paper.

74 **Structural Geology of Endeavour Crater**

75 Endeavour is a complex impact crater that is largely buried by younger sulfate-rich
76 sandstones of the Burns formation (Squyres et al. 2012; Crumpler et al. 2015; Grant et al. 2015).
77 The exposed rim is divided into discrete segments separated by relatively low regions covered by
78 Burns formation rocks. The presence of extensive breccia outcrops of the Shoemaker formation
79 on Cape York and Murray Ridge confirms that the crater formed by a bolide impact (Squyres et al.
80 2012; Arvidson et al. 2014; Crumpler et al. 2015). Comparison to Martian impact craters of
81 similar size indicates that only ~100 to 200 m of rim material has been removed by erosion,
82 mostly by fluvial activity before deposition of Burns formation materials (Grant et al. 2015).
83 Thus, exploration and characterization of Endeavour's rim by Opportunity provide detailed ground
84 truth information about the lithologic nature and extent of alteration by aqueous fluids for the rim
85 of a Noachian-age complex impact crater.

86 Structural observations of complex terrestrial impact craters similar in size to Endeavour
87 provide insight into the types of fractures expected on the rim segments and surrounding terrains
88 explored by Opportunity. In particular, the Ries Crater, which is ~26 km in diameter (Stöffler et al.
89 2013), the ~23 km diameter Haughton Crater (Osinski and Spray 2005), and the ~22 km wide
90 Gosses Bluff impact structure (Milton et al. 1972) have been studied in detail, and exhibit
91 extensive fractures that formed both radially and concentrically to the crater centers. Osinski and
92 Spray (2005) and Kenkmann et al. (2014) provide schematic views of structural patterns generated
93 during the collapse stage of complex crater formation. Their models, supported by observations,
94 imply that concentric and radial fractures should cut through rim structures of complex craters.
95 These fractures should also propagate upward through deposits generated after the impact event by
96 reactivation during later local- to regional-scale tectonic activity and/or increased stresses
97 associated with loading as later deposits accumulate.

98 Mars Reconnaissance Orbiter HiRISE images offer 0.25 m/pixel ground resolution, with
99 an imaging system modulation transfer function that preserves fine spatial details of the Martian
100 surface (McEwen et al. 2007). Examination of HiRISE images for Endeavour rim and inter-rim
101 segments traversed by Opportunity show evidence for both concentric and radial fractures,
102 including systems that have propagated upward into Burns formation materials. For example, the
103 Burns formation bedrock in Botany Bay hosts fractures that are approximately parallel or
104 perpendicular to the rim segments (Fig. 3). In addition, several fractures are evident extending
105 westward from Murray Ridge into the surrounding Burns formation materials (Fig. 4). As will be
106 shown in the next section of this paper, Opportunity-based images demonstrate that the impact
107 breccia outcrops on Murray Ridge exhibit extensive fracturing that is consistent with the formation
108 of Endeavour Crater and later readjustments.

109

110
111
112
113
114
115
116
117
118
119
120
121
122
123
124
125

126
127
128
129
130
131
132

Opportunity's Exploration of Murray Ridge

Opportunity traversed from outcrops of Burns formation sandstones onto the Shoemaker and underlying Matijevic formation rocks (Squyres et al., 2012; Arvidson et al., 2014; Crumpler et al., 2015) exposed on the Cape York rim segment of Endeavour Crater in 2011. The rover explored this rim segment until it was commanded to head south and enter Botany Bay. Opportunity then crossed the Burns formation outcrops in Botany Bay and approached its first outcrop on the northeastern corner of Murray Ridge (Fig. 1). After conducting several measurements on this portion of the rim, Opportunity was commanded to drive around the northern nose of Murray Ridge (Solander Point) and begin extensive exploration and characterization of its western slopes. The western side of Murray Ridge was chosen because of extensive outcrops and less steep terrain than the interior portion of the Ridge. Opportunity is a solar-powered rover located in the southern hemisphere. As a consequence, the rover is subject to low solar power during the southern winter season, and its activities are more limited than during other seasons. For its sixth winter season Opportunity was directed to Cook Haven, a gentle swale on Murray Ridge (Fig. 4) with requisite north-facing slopes that would provide enough solar power for the rover to survive and gather some science data.

Opportunity's exploration and characterization of outcrops on Murray Ridge included imaging using Pancam and the engineering cameras, with a number of stops for measurements of breccia and soil targets using the MI and APXS instruments. Table 1 provides APXS compositions for Murray Ridge targets covered in this paper. Two key stops for remote sensing and compositional measurements to the north of Cook Haven were the Spinifex outcrop target and, farther south, the Moreton Island area, with its Mount Tempest and Tangalooma outcrop targets (Fig. 5). At both sites these breccia outcrops exhibit extensive fractures. These breccia outcrops

133 contain relatively dark rock clasts several centimeters in diameter embedded in a relatively
134 brighter, fine-grained matrix. The targets were too rough to brush or grind using the RAT.

135 After leaving Moreton Island, Opportunity traversed into Cook Haven from the south,
136 thereby avoiding the need to cross south-facing slopes and low insolation values associated with
137 the northern portion of this gentle swale. Imaging of Cook Haven shows low-lying, relatively
138 bright outcrops cut by fractures that are partially filled with wind-blown soil deposits (Fig. 6-7).
139 During the downhill traverse into Cook Haven Opportunity stopped on a soil-filled fracture, later
140 executing a 146-degree turn, with the rear and middle wheels unintentionally excavating both the
141 soil and underlying rocks (Figs. 7-8). Two rocks, subsequently named Pinnacle Island and Stuart
142 Island (PI and SI), were fortuitously excavated and overturned to reveal unusually dark and bright
143 material on the newly exposed rock surfaces. PI slid within reach of Opportunity's IDD after the
144 rover completed its drive and was conducting measurements on the Cape Darby outcrop, requiring
145 no additional rover motions to deploy the MI and APXS onto the newly arrived ~3.5 cm wide
146 rock. Opportunity conducted measurement campaigns on both PI and SI, the soil (named Anchor
147 Point) from which they were excavated, and a loose, relatively dark rock cobble in the vicinity
148 named Sledge Island. Bedrock outcrops Cape Elizabeth and Green Island, both flat outcrops that
149 were brushed before MI and APXS data were acquired (Fig. 8-9), illustrate the nature of outcrops
150 in Cook Haven in that they are relatively bright compared to other Murray Ridge outcrops, with
151 small rock clasts set in an extensive, fine-grained matrix. On the way out of Cook Haven during
152 the ensuing southern hemisphere spring season, Opportunity conducted measurements on one last
153 Cook Haven outcrop, a target named Turnagain Arm, and then exited Cook Haven to continue
154 exploring the western portion of Murray Ridge.

155 A breccia outcrop named Bristol Well located to the south of Cook Haven exhibited bright
156 veins within fractures (Fig. 10). Three overlapping APXS and MI measurements were acquired to

157 either side and centered on one of the veins. In-situ measurements were also made on impact
158 breccia targets to the south of the Bristol Well targets. These targets are the Sarcobatus outcrop
159 matrix and two overlapping measurements on a relatively dark rock clast (Fig. 11). The matrix
160 target was flat and smooth, enabling brushing before acquiring MI and APXS data. The last two
161 breccia targets on Murray Ridge were Tuscaloosa and Sodaville. The former represents outcrop
162 and the latter grus-like debris within a fracture just uphill of Tuscaloosa. After these measurements
163 the rover continued south, conducting its last in-situ measurements on a soil target named
164 Barstow, and left Murray Ridge to begin its ascent of the Cape Tribulation rim segment (Fig. 1).

165 **Murray Ridge Outcrop and Soil Compositional Trends**

166 APXS compositional data in Table 1 show that Murray Ridge rocks and soils are basaltic
167 in composition, with the notable exceptions of the Bristol Well vein and the relatively dark and
168 bright materials associated with PI and SI rocks excavated by Opportunity's wheels. To evaluate
169 further the extent to which there are deviations toward smectite or other phyllosilicate
170 compositions similar to what was found on Cape York (Arvidson et al. 2014), APXS data for
171 outcrops and soils (excluding PI and SI) are shown in a ternary plot of mole fraction Al_2O_3 –
172 $(\text{CaO}+\text{Na}_2\text{O}+\text{K}_2\text{O})$ – $(\text{FeO}_T+\text{MgO})$ (Fig. 12). Also plotted are laboratory-based measurements for
173 various phyllosilicates and other APXS data for Endeavour's rim. The Espérance data are for
174 APXS measurements at Cape York in a fracture zone where progressively deeper RAT grinds
175 showed evidence for a compositional trend toward montmorillonite (Arvidson et al. 2014). With
176 the exception of the Bristol Well and Sledge Island measurements, no significant deviations from
177 a narrow range of basaltic compositions are evident. Examination of data shown in Table 1
178 demonstrates that Sledge Island has a slightly different composition as compared to outcrops on
179 Murray Ridge and may be an erratic added to Cook Haven (e.g., as impact ejecta).

180 The Bristol Well vein is ~1 cm wide and did not fill the field of view of the APXS. Three
181 overlapping in-situ measurements were made in a direction perpendicular to the vein in attempt to
182 determine vein composition, using the methodology implemented for measurements over the
183 Homestake vein on Cape York (Squyres et al. 2012). The Bristol Well_2 target was centered over
184 the vein and shows slightly enhanced values of Ca and S and lower values of Fe, Si, Al, and Mg as
185 compared to Bristol Well 1 and 3 targets (Table 1). Similar compositional patterns were found for
186 the Homestake vein that cuts the Grasberg bench deposits surrounding Cape York. Both the
187 Homestake and Bristol Well data, and the Ortiz vein measurements on Matijevec Hill (Cape York)
188 (Arvidson et al., 2014), indicate that sulfate-rich aqueous fluids moved through fractures and
189 precipitated relatively insoluble a Ca sulfate mineral or minerals during one more episodes.

190 The Cook Haven bedrock exposures are brighter, relatively flat-lying, and have smaller
191 lithic clasts than other breccia outcrops on Murray Ridge. These outcrops have more S and Cl than
192 the other breccia outcrop targets on the ridge (Fig. 13). This is the case even after brushing to
193 remove loose dust and sand. In addition, the Sarcobatus brushed breccia matrix target shows an
194 enrichment of Cl relative to other Murray Ridge rocks, including the Sarcobatus clast. The
195 increase in S and Cl is interpreted to be due to the slight addition by aqueous processes of sulfate
196 and chloride salts to selected Murray Ridge rocks, primarily to Cook Haven bedrock. The
197 compositional trends shown in Fig. 13 also highlight the very high S content of PI and SI rocks.
198 We consider in detail textures and compositions, together with inferred mineral phases, and
199 explanations for the high S content of these two rocks in the next several sections of this paper.

200 **Pinnacle and Stuart Island Rock Coatings as Observed by Pancam and the Microscopic** 201 **Imager**

202 Pancam false color images, together with MI anaglyphs generated from stereo observations
203 by varying the IDD incoming angle to produce image pairs with parallax (Herkenhoff et al. 2006),

204 show that the PI and SI rocks are thinly coated by dark materials (Figs. 14-17). In addition, PI
205 shows evidence for a thin, bright coating interpreted to lie directly on top of relatively fresh rock
206 surfaces and beneath the dark coating (Fig. 14-17). The dark coating is concentrated in the
207 concave-upward center part of PI and has a lumpy texture. Pancam false color images, combined
208 with MI data (Figs. 16-17), indicate that SI does not exhibit the same type of areal extensive,
209 relatively bright coating found on PI. Instead in the false color images and MI data, SI exhibits an
210 extensive and variably colored dark coating, together with areas interpreted to be relatively fresh
211 or dusty rock surfaces. The former have a bluish-gray and the latter a reddish hue. MI anaglyphs
212 covering SI do show several oval-shaped areas that are interpreted to be rock clasts, with one of
213 them surrounded by a very thin, relatively bright annulus (Fig. 16). The bright annulus, in turn, is
214 surrounded by a relatively dark annulus. Thus both PI and SI exhibit dark coatings, with a bright
215 coating well exposed on PI.

216 Pancam 13-band multispectral observations (0.432 to 1.009 μm) acquired for PI, SI and
217 surrounding areas provide quantitative colorimetric and spectral reflectance constraints on coating
218 mineralogy. Pancam raw image data were calibrated to surface radiance factor (I/F , where I is the
219 measured radiance and πF is the incident solar radiance) divided by the cosine of the incidence
220 angle at the time of image acquisition, with absolute reflectance levels accurate to within $\sim 10\%$
221 (Bell et al. 2006). Spectral endmembers for PI were retrieved using the sequential maximum
222 angle convex cone methodology in which spectral extremes are located in multidimensional space
223 and separated from shadow values (Gruninger et al. 2004). Four statistically significant
224 endmembers were retrieved: relatively fresh rock, dusty rock bright coating, and dark coating (Fig.
225 18).

226 The dusty rock endmember spectrum has a broad ferric edge absorption ($\sim 0.43\text{-}0.75 \mu\text{m}$)
227 interpreted to result from Fe^{3+} in nanophase iron oxides found in Martian dust (Morris et al. 1993).

228 The fresh rock endmember spectrum resembles the spectral properties of rocks on Murray Ridge
229 not covered or only thinly covered by dust. The ferric edge is subdued relative to the dusty rock
230 spectrum, and at longer wavelengths the spectrum shows a shallow dip, consistent with electronic
231 absorptions due to the presence of one or more ferrous silicates, most likely pyroxene(s) (Clark
232 1999). The bright coating endmember has the highest reflectance values of the four PI
233 endmembers. The ferric edge is present, but not as prominent as observed for the dusty rock. The
234 bright coating endmember spectrum also exhibits a relatively steep downturn in reflectance
235 between 0.9 to 1.0 μm , consistent with the presence of H_2O and/or OH in the mineral structure
236 (e.g., Rice et al. 2010).

237 Spectral endmembers were retrieved using the sequential maximum angle convex cone
238 methodology on Pancam 13-band data for SI. Four endmembers were entered as a constraint,
239 although only three could be retrieved in a statistically viable manner. The first is similar to the PI
240 dusty rock endmember, and the second is similar to the relatively fresh rock endmember. The third
241 is statistically indistinguishable from the PI dark coating endmember (Fig. 18). The PI and SI
242 dark coating endmember spectra both have very low reflectance values that increase
243 monotonically with increasing wavelength, with the exception of a shallow dip centered at 0.754
244 μm , and a flattening of the slope for wavelengths longer than 0.934 μm . Munsell color values
245 (Kelly and Judd 1976) for the dark coating endmembers for both rocks are 2.5R2.5/2, where 2.5R
246 designates a slight deviation from a red hue, 2.5 indicates a dark surface, and 2 indicates a near
247 gray appearance. The dark coating endmember color and spectral properties are unique for Mars,
248 which ubiquitously show ferric absorptions at shorter wavelengths, increasing rapidly with
249 increasing wavelength to $\sim 0.77 \mu\text{m}$, as shown for the other endmember spectra. We revisit the
250 likely mineralogy of the dark and bright coatings after first considering constraints from the
251 APXS-based compositions for PI and SI rocks.

252 **Pinnacle and Stuart Island Compositions and Endmember Retrievals**

253 Five overlapping APXS observations were acquired for PI (Fig. 14) and four for SI (Fig.
254 16) (Table 1). The field of view (FOV) of the instrument is comparable to the ~3.5 cm PI width,
255 although most of the signal comes from the inner portion of the FOV. The situation is slightly
256 better for the ~12 cm long SI rock. APXS placements were positioned to concentrate on the
257 spectral endmember locations for PI and to cover the breadth of SI. For the PI APXS
258 measurements the highly overlapping nature of the observations requires that care be taken in
259 interpretation. Examination of the compositional data shown in Table 1 shows enrichments in
260 Mg, Mn, Ni, and S for both PI and SI, relative to surrounding basaltic bedrock. The enrichment
261 patterns are also distinctly different than found for the sulfate-rich sandstones that dominate the
262 Burns formation (Clark et al. 2005). The APXS FOVs containing the highest concentrations of the
263 dark coating endmember (PI_3, PI_5) have the greatest enrichments in these elements. PI_3 and
264 PI_5 also show minor enrichments in Ca and P, and overall the PI targets have higher
265 concentrations of Cl, relative to SI targets (Fig. 13, Table 1). PI_3 has the highest concentration of
266 Mn (3.48 wt% MnO, Table 1) measured by the Spirit and Opportunity rovers, and SI_3 has the
267 highest S concentration (38.21 wt% SO₃, Table 1) measured by either rover. PI and SI coating
268 compositions are thus unique among the many hundreds of APXS measurements collected by the
269 Spirit and Opportunity rovers (Gellert et al. 2006).

270 Because the APXS FOV is large relative to the size of PI, it is not possible to use the
271 observations alone to retrieve the compositions of the purest dark and bright coatings that are well-
272 exposed on this rock and localized using Pancam spectral analysis. On the other hand, if we
273 assume that the compositions follow the areal concentrations of Pancam-based endmembers,
274 various techniques can be used to retrieve compositional estimates for the purest endmember
275 locations. To pursue these retrievals, the location of each APXS PI measurement was derived from

276 examination of MI frames pointed toward the APXS target center, together with projections of the
277 IDD motions toward the target. Locations were refined using the predicted total signal as a
278 function of terrain topography and derived APXS stand-off distances. Overall the methodology for
279 localization of the APXS measurements followed the procedures described in VanBommel et al.
280 (2016).

281 For each PI APXS observation the Pancam-based endmember phase abundance maps were
282 spatially convolved with the APXS FOVs at the Pancam pixel scale, given the APXS
283 measurement location, the lateral distance from the detector center, the APXS detector stand-off
284 distance, and topography (Fig. 19). To ensure more observations than unknowns in retrieving
285 compositions for the Pancam-based purest endmember locations, the dusty and fresh rock
286 endmembers were combined, and SI, Anchor Point soils, and Cook Haven bedrock observations
287 were added to the data matrix. Thus sixteen measurements were used together with the phase
288 abundance matrix (three endmember columns and sixteen observation rows) to solve for the
289 compositions of three endmembers (sixteen oxide columns and three endmember rows): rock,
290 bright coating, and dark coating. In matrix notation the phase abundance matrix was post-
291 multiplied by the endmember composition matrix to generate the matrix of oxide compositions.

292 An iterative minimization algorithm with a non-negativity constraint was used in which
293 both the phase abundance and endmember composition matrix values were allowed to vary. Initial
294 phase abundances for PI observations were set by the Pancam-based endmember map
295 convolutions with the APXS FOVs, whereas the other initial phase abundances were initially set
296 to random numbers, including those for SI. The sums of squared deviations between the model
297 predictions and measured values for the sixteen elements for the sixteen APXS measurements
298 were minimized and used to compute statistical errors of the retrieved endmember compositions
299 and phase abundances. Results are presented in Table 2 for retrieved endmember compositions

300 and Table 3 for phase abundances. Major elements were retrieved with small errors for the dark
301 coating and rock endmembers. The bright coating endmember composition retrievals have
302 relatively large errors that are a consequence of the small areal extent of this endmember and thus
303 relatively poor APXS statistics. Low concentration elements were also difficult to retrieve for all
304 endmembers and some zero values were retrieved, which is compositionally incorrect, and a
305 limitation of the retrieval procedure. Phase abundance retrievals are consistent with the Pancam-
306 based images for PI, e.g., examinations of APXS locations over the endmember abundance maps
307 are consistent with retrievals shown in Table 3. In addition, SI phase abundances show high
308 concentrations of bright and dark endmembers in all four observations, consistent with the more
309 complicated color patterns evident in Pancam data for SI than for PI (Figs. 14 and 16).

310 To pursue how the endmember retrievals match and/or extend trends in compositions, a
311 correspondence analysis (CA) was run for all measurements on Murray Ridge and included the
312 three endmember compositions (Fig. 20). CA is a row- and column-normalized principal
313 component analysis used for understanding correlations among samples and variables and has
314 been used to explore patterns for the intrinsically multivariate APXS data acquired by both the
315 Spirit and Opportunity rovers (Arvidson et al. 2010, 2011). The first two CA factor loadings,
316 which carry ~98% of the data variance, demonstrate that the rock endmember composition has a
317 close affinity to bedrock. The bright and dark coating endmembers extend the differences in
318 compositions between the measurements centered over the bright and dark coating exposures on
319 PI. The bright coating endmember is characterized by an affinity for magnesium and sulfur, and
320 modest amounts of manganese, whereas the dark coating also has an affinity for manganese,
321 calcium, and phosphorus, in addition to magnesium and sulfur.

322 We also use the trends evident in the CA factor loadings plot to consider bivariate
323 correlations between oxide compositions, e.g., Si and S are clearly negatively correlated (Fig. 20).

324 This is evident in a plot and high correlation coefficient of these two elemental abundances (Fig.
325 21). Mg and S are positively correlated as are Ca and P (Figs. 20-21). The retrieved rock and dark
326 coating endmembers bound the first three bivariate plots, whereas the Ca vs P plot shows a much
327 greater spread of data and endmembers. Ni is not well estimated in the endmember retrievals.
328 However, a strong Mn vs. Ni positive correlation is evident in the bivariate plot shown in Fig. 22,
329 using only the actual APXS observations.

330 **Inferred Pinnacle Island Bright and Dark Coating Mineral Phases**

331 The bright endmember coating spectral reflectance is consistent with the presence of a pure
332 Mg-sulfate endmember, although the composition, low overall reflectance relative to Mg sulfate
333 powders and rocks (e.g., Cloutis et al. 2006), and the presence of the short wavelength ferric
334 absorption imply a more complex mineral assemblage. The dark coating endmember spectral
335 characteristics are clearly indicative of the presence of one or more minerals that are intrinsically
336 dark because of multiple, overlapping charge transfer and/or electronic transition absorptions
337 associated with the presence of transition metals such as Mn (Sherman 1984). We explore a range
338 of possible candidates to show that the low reflectance and lack of ferric edge are consistent with
339 the presence of Mn oxides. A number of synthetic samples were generated and used to pursue this
340 comparison, including hausmannite ($(\text{Mn}^{2+}, \text{Mn}^{3+})_2\text{O}_4$), bixbyite ($\alpha\text{-Mn}^{3+}_2\text{O}_3$), pyrolusite ($\beta\text{-Mn}^{4+}\text{O}_2$),
341 a series of phylломanganates: triclinic and hexagonal forms of birnessite ($(\text{Na}, \text{Ca}, \text{K})_x(\text{Mn}^{4+}, \text{Mn}^{3+})_2\text{O}_4 \cdot n\text{H}_2\text{O}$), and vernadite ($\text{Na}_{0.2}\text{Mn}^{4+}_{0.95}\text{O}_2 \cdot n\text{H}_2\text{O}$). These phases were synthesized
342 in the laboratory under controlled conditions, with phase identification verified using X-ray
343 diffraction (Hinkle 2015). Spectral reflectance data were acquired for silt-sized portions of these
344 minerals with lighting and viewing conditions similar to those for which the Pancam data were
345 acquired (Fig. 23). All of the Mn oxide spectra have low overall values and either are spectrally
346 flat, or increase modestly in reflectance with increasing wavelength, consistent with the
347

348 overlapping nature of the charge transfer and electronic transition absorptions for these oxides. To
349 our knowledge no other Mn-bearing minerals (e.g., Mn sulfates, which are bright pink) exhibit
350 these spectral characteristics. Mn sulfides were not considered to be viable matches for the dark
351 coating endmember spectra because these minerals are exceptionally rare in nature. The reason is
352 that the electronic structure of Mn favors the maintenance of localized 3d orbitals in a high-spin
353 configuration, rather than hybridization into molecular orbitals shared with sulfur and typical of
354 other sulfide minerals (Vaughan and Rosso 2006).

355 To further pursue possible mineral assemblages we calculated the phases that would have
356 been produced if the bright and dark coating endmember compositions formed via equilibrium
357 precipitation from an aqueous fluid. Calculations were based on a geochemical reaction model
358 using The Geochemist's Workbench version 10.0.6 (Bethke 2007). Oxide components reported in
359 Table 2 were modeled as reacting with 1 kg of water, converting to mineral phases based on fluid
360 saturation state. Cr₂O₃, Br, Ni, and Zn were excluded from the model as these occur at minor to
361 trace levels and will largely occur as substituting elements in other minerals. Reaction of 1.5 kg of
362 oxide components with 1 kg of water yielded a stable configuration, i.e., an incremental addition
363 of oxide components yielded a proportional increase in existing minerals. This reaction left a
364 residual brine containing primarily Mg and sulfate; this fluid was then evaporated to obtain the full
365 mineralogy. The initial reaction employed a previously-described thermodynamic database
366 (Catalano 2013). The evaporation step required use of a Pitzer-style activity model. A previously-
367 compiled database (Tosca et al. 2005, 2007) was modified with more recent compilations of ion-
368 interaction parameters (Marion et al. 2003, 2008, 2009, 2010) and revised solubility data (Grevel
369 and Majzlan 2009, 2011; Kobylin et al. 2011; Majzlan et al. 2004a, 2004b). Pitzer models are not
370 parameterized for P and Ti, and thus these elements were removed for the evaporation step;
371 >99.99% of the P and Ti added to the system were precipitated in minerals in the initial reaction.

372 All calculations were performed at 25°C because the thermodynamic data available is most robust
373 at this temperature.

374 The geochemical modeling results yield plausible mineral assemblages, with both
375 endmembers dominated by Mg sulfate, as expected from the bulk compositions (Fig. 24). The
376 dark coating endmember retrieval also contains gypsum, ferric hydroxysulfates, and ferric
377 phosphate, with the bright coating retrieval containing nontronite (as the main host of SiO₂), and
378 minor gibbsite and gypsum. Mn in both coatings is predicted to occur as a phyllomanganate
379 (birnessite), with the dark coating containing a substantially larger mass fraction of this mineral.
380 These calculations assume all phases were in equilibrium and that the endmembers contained no
381 detrital material. Neither assumption is fully valid for real systems. Thus these calculated
382 assemblages simply demonstrate that endmember compositions correspond to realistic mineral
383 assemblages that would form by precipitation from aqueous solutions. Additional calculations
384 (not shown) explored possible paragenetic sequences associated with closed system chemical
385 processes during and after deposition, but were unable to produce the dark coatings by alteration
386 or leaching of the bright coatings, and vice versa, as both contain mixtures of soluble and
387 insoluble phases and have distinct compositions. The model results suggest that the formation of
388 these coatings involved multiple stages of fluid flow and coating formation.

389 **Formation and Uniqueness of Pinnacle and Stuart Island Coatings**

390 The morphologic, stratigraphic, spectral, and compositional patterns evident on the PI and
391 SI rock surfaces are interpreted to indicate two episodes of authigenic mineral deposition, both
392 dominated by precipitation of sulfates from subsurface fluids that were largely neutralized by
393 reactions with basaltic bedrock. The initial precipitation generated bright coatings that were
394 subsequently altered to form a thin layer of what is likely Mg-sulfate-dominated mineralogy that

418 Endeavour's Murray Ridge rim segment do not show major element compositional deviations
419 from a basaltic composition. Minor fracture-filling Ca-sulfate veins have been encountered,
420 implying modest flow of fluids and regional-scale precipitation of a relatively insoluble sulfate
421 phase or phases. In addition, relatively high S and Cl concentrations associated with Cook Haven
422 bedrock outcrops imply modest addition of these mobile elements. On the other hand, Pinnacle
423 and Stuart Island rocks, serendipitously excavated from a soil-filled fracture by Opportunity's
424 wheels, provide strong evidence for movement of fluids through the subsurface, and formation of
425 a unique sulfate-rich deposit overlain by a sulfate and Mn oxide-rich coating.

426 On the basis of inferred mineralogy, the aqueous fluids that deposited coatings on Pinnacle
427 and Stuart Island rocks exhibited temporally varying redox conditions governed by subsurface
428 rock-water interactions in contact with an oxidizing surface environment. Discovery of these rare
429 deposits on the rim of Endeavour Crater complements the discovery of equally rare Mn-oxide
430 deposits formed by aqueous flow in subsurface fractures by the Curiosity rover in Gale Crater
431 (Lanza et al. 2015). These two discoveries demonstrate that Mn-oxides must have been part of the
432 planet's secondary mineral repertoire that required a stronger redox gradient in some near-surface
433 environments than previously recognized. In contrast to arid regions on Earth, where Mn oxides
434 are widely incorporated into coatings on surface rocks (e.g., Liu and Broecker 2008), our results
435 demonstrate that on Mars the most likely place to deposit and preserve Mn oxides was in fracture
436 zones where migrating fluids intersected surface oxidants, forming precipitates shielded from
437 subsequent physical erosion.

438

439

Acknowledgements

440 We thank the Opportunity Project Team at the NASA/Caltech Jet Propulsion Laboratory
441 and scientists from many institutions who made possible the collection of data included in this
442 paper. We thank Paolo Bellutta for help in localizing APXS fields of view and Susan Slavney and
443 Jennifer Ward for careful review and editing of text and figures. Bonnie Redding, United States
444 Geological Survey, kindly generated the MI anaglyphs. We also thank NASA for the support
445 needed to operate Opportunity and collect and analyze the data included in this paper and the Mars
446 Fundamental Research Program support to J. G. Catalano. The NASA Planetary Data System
447 Geosciences Node houses the data included in this paper and we thank them for their efforts. See:
448 <http://pds-geosciences.wustl.edu/>.

449

450

References

- 451 Arvidson, R.E., Bell, J.F. III, Bellutta, P., Cabrol, N.A., Catalano, J.G., Crumpler, L., Des Marais,
452 D.J., Estlin, T., Farrand, W., Gellert, R., and others (2010) Spirit Mars Rover mission:
453 Overview and selected results from the northern Home Plate Winter Haven to the side of
454 Scamander crater. *Journal of Geophysical Research: Planets*, 115, E00F03,
455 doi:10.1029/2010JE003633.
- 456 Arvidson, R.E., Ashley, J.W., Bell, J.F. III, Chojnacki, M., Cohen, J., Economou, T.E., Farrand,
457 W.H., Ferguson, R., Fleischer, I., Geisler, P., and others (2011) Opportunity Mars Rover
458 mission: Overview and selected results from Purgatory ripple to traverses to Endeavour
459 crater. *Journal of Geophysical Research: Planets*, 116, E00F15, doi:2010JE003746.
- 460 Arvidson, R.E., Squyres, S.W., Bell, J.F., Catalano, J.G., Clark, B.C., Crumpler, L.S., de Souza,
461 P.A., Fairén, A.G., Farrand, W.H., Fox, V.K., and others (2014) Ancient aqueous
462 environments at Endeavour crater, Mars. *Science*, 343, doi:10.1126/science.1248097.
- 463 Bell, J.F., Squyres, S.W., Herkenhoff, K.E., Maki, J.N., Arneson, H.M., Brown, D., Collins, S.A.,
464 Dingizian, A., Elliot, S.T., Hagerott, E.C., and others (2003) Mars Exploration Rover Athena
465 Panoramic Camera (Pancam) investigation. *Journal of Geophysical Research: Planets*, 108,
466 8063, doi:10.1029/2003JE002070, E12.
- 467 Bell, J.F. III, Joseph, J., Sohl-Dickstein, J.N., Arneson, H.M., Johnson, M.J., Lemmon, M.T., and
468 Savransky, D. (2006) In-flight calibration and performance of the Mars Exploration Rover
469 Panoramic Camera (Pancam) instruments. *Journal of Geophysical Research*, 111, E02S03,
470 doi:10.1029/2005JE002444.

- 471 Bethke, C.M. (2007) *Geochemical and Biogeochemical Reaction Modeling*, 547 p. Cambridge
472 University Press, New York.
- 473 Catalano, J.G. (2013) Thermodynamic and mass balance constraints on iron-bearing phyllosilicate
474 formation and alteration pathways on early Mars. *Journal of Geophysical Research: Planets*,
475 118, 2124-2136, doi:10.1002/jgre.20161.
- 476 Clark, B.C., Morris, R.V., McLennan, S.M., Gellert, R., Jolliff, B., Knoll, A.H., Squyres, S.W.,
477 Lowenstein, T.K., Ming, D.W., Tosca, N.J., and others (2005) Chemistry and mineralogy of
478 outcrops at Meridiani Planum. *Earth and Planetary Science Letters*, 240, 73-94,
479 doi:10.1016/j.epsl.2005.09.040.
- 480 Clark, R. (1999) Chapter 1: Spectroscopy of rocks and minerals, and principles of spectroscopy. In
481 A.N. Rensz, Ed., *Remote Sensing for the Earth Sciences Vol. 3*, pp. 3-58. John Wiley and
482 Sons, New York.
- 483 Cloutis, E.A., Hawthorne, F.C., Mertzman, S.A., Krenn, K., Craig, M.A., Marcino, D., Methot,
484 M., Strong, J., Mustard, J.F., Blaney, D.L., Bell, J.F. III, and Vilas, F. (2006) Detection and
485 discrimination of sulfate minerals using reflectance spectroscopy. *Icarus*, 184, 121-157,
486 doi:10.1016/j.icarus.2006.04.003.
- 487 Crumpler, L.S., Arvidson, R.E., Bell, J., Clark, B.C., Cohen, B.A., Farrand, W.H., Gellert, R.,
488 Golombek, M., Grant, J.A., Guinness, E., and others (2015) Context of ancient aqueous
489 environments on Mars from in situ geologic mapping at Endeavour Crater. *Journal of*
490 *Geophysical Research: Planets*, 120, 538-569, doi:10.1002/2014JE004699.
- 491 Ehlmann, B.L., and Edwards, C.S. (2014) Mineralogy of the Martian surface. *Annual Review of*
492 *Earth and Planetary Sciences*, 42, 291-315, doi:10.1146/annurev-earth-060313-055024.

- 493 Emmerich, K., Wolters, F., Kahr, G., and Lagaly, G. (2009) Clay profiling: The classification of
494 montmorillonites. *Clays and Clay Minerals*, 57, 104-114, doi:10.1346/CCMN.2009.0570110.
- 495 Fox, V., Arvidson, R., Squyres, S., and Murchie, S. (2014) Smectites in the rim of Endeavour
496 crater, Mars, detected using along-track oversampled CRISM observations. American
497 Geophysical Union, Fall Meeting 2014, Abstract P41A-3882.
- 498 Gellert, R., Rieder, R., Brückner, J., Clark, B.C., Dreibus, G., Klingelhöfer, G., Lugmair, G.,
499 Ming, D.W., Wänke, H., Yen, A., and others (2006) Alpha Particle X-ray Spectrometer
500 (APXS): Results from Gusev crater and calibration report. *Journal of Geophysical Research:*
501 *Planets*, 111, E02S05, doi:10.1029/2005JE002555.
- 502 Gorevan, S.P., Myrick, T., Davis, K., Chau, J.J., Bartlett, P., Mukherjee, S., Anderson, R.,
503 Squyres, S.W., Arvidson, R.E., Madsen, M.B., and others (2003) Rock Abrasion Tool: Mars
504 Exploration Rover mission. *Journal of Geophysical Research: Planets*, 108, 8068,
505 doi:10.1029/2003JE002061, E12.
- 506 Grant, J.A., Parker, T.J., Crumpler, L.S., Wilson, S.A., Golombek, M.P., and Mittlefehldt, D.W.
507 (2015) The degradational history of Endeavour Crater, Mars. *Icarus*,
508 doi:10.1016/j.icarus.2015.08.019, in press.
- 509 Grevel, K.D., and Majzlan, J. (2009) Internally consistent thermodynamic data for magnesium
510 sulfate hydrates. *Geochimica et Cosmochimica Acta*, 73(22), 6805-6815,
511 doi:10.1016/j.gca.2009.08.005.
- 512 Grevel, K.D., and Majzlan, J. (2011) Internally consistent thermodynamic data for metal divalent
513 sulphate hydrates. *Chemical Geology*, 286(3-4), 301-306,
514 doi:10.1016/j.chemgeo.2011.05.016.

- 515 Grotzinger, J.P., Sumner, D.Y., Kah, L.C., Stack, K., Gupta, S., Edgar, L., Rubin, D., Lewis, K.,
516 Schieber, J., Mangold, N., and others (2014) A habitable fluvio-lacustrine environment at
517 Yellowknife Bay, Gale Crater, Mars. *Science*, 343, doi:10.1126/science.1242777.
- 518 Grotzinger, J.P., Gupta, S., Malin, M.C., Rubin, D.M., Schieber, J., Siebach, K., Sumner, D.Y.,
519 Stack, K.M., Vasavada, A.R., Arvidson, R.E., and others (2015) Deposition, exhumation, and
520 paleoclimate of an ancient lake deposit, Gale crater, Mars. *Science*, 350,
521 doi:10.1126/science.aac7575.
- 522 Gruninger, J.H., Ratkowski, A.J., and Hoke, M.L. (2004) The sequential maximum angle convex
523 cone (SMACC) endmember model. In S.S. Shen and P.E. Lewis, Eds., *Proceedings SPIE,*
524 *Algorithms and Technologies for Multispectral, Hyperspectral, and Ultraspectral Imagery X,*
525 5425, doi:10.1117/12.543794, Orlando, Florida.
- 526 Herkenhoff, K.E., Squyres, S.W., Bell, J.F., Maki, J.N., Arneson, H.M., Bertelsen, P., Brown,
527 D.I., Collins, S.A., Dingizian, A., Elliott, S.T., and others (2003) Athena Microscopic Imager
528 investigation. *Journal of Geophysical Research: Planets*, 108, 8065,
529 doi:10.1029/2003JE002076, E12.
- 530 Herkenhoff, K.E., Squyres, S.W., Anderson, R., Archinal, B.A., Arvidson, R.E., Barrett, J.M.,
531 Becker, K.J., Bell, J.F. III, Budney, C., Cabrol, N.A., and others (2006), Overview of the
532 Microscopic Imager Investigation during Spirit's first 450 sols in Gusev crater. *Journal of*
533 *Geophysical Research: Planets*, 111, E02S04, doi:10.1029/2005JE002574.
- 534 Hinkle, M.A.G. (2015) Ion interactions at the mineral-water interface during biogeochemical iron
535 and manganese cycling, Ph.D. thesis, Washington University in St. Louis,
536 doi:10.7936/K7JQ0Z58.

- 537 Kelly, K.L., and Judd, D.B. (1976) Color: Universal Language and Dictionary of Names, 196 p.
538 U.S. Department of Commerce, National Bureau of Standards.
- 539 Kenkmann, T., Poelchau, M.H., and Wulf, G. (2014) Structural geology of impact craters. Journal
540 of Structural Geology, 62, 156-182, doi:10.1016/j.jsg.2014.01.015.
- 541 Klein, C. (2002) The 22nd Edition of the Manual of Mineral Science, 641 pp., John Wiley & Sons,
542 New York.
- 543 Kobylin, P.M., Sippola, H., and Taskinen, P.A. (2011) Thermodynamic modelling of aqueous
544 Fe(II) sulfate solutions. CALPHAD: Computer Coupling of Phase Diagrams and
545 Thermochemistry, 35(4), 499-511, doi:10.1016/j.calphad.2011.08.005.
- 546 Lanza, N. et al. (2015) Understanding the signature of rock coatings in laser-induced breakdown
547 spectroscopy data. Icarus 249, 62-73, doi:10.1016/j.icarus.2014.05.038.
- 548 Liu, T., and Broecker, W.S. (2008) Rock varnish evidence for latest Pleistocene millennial-scale
549 wet events in the drylands of Western United States. Geology, 36, 403-406,
550 doi:10.1130/G24573A.1.
- 551 Majzlan, J., Navrotsky, A., and Schwertmann, U. (2004a) Thermodynamics of iron oxides: Part
552 III. Enthalpies of formation and stability of ferrihydrite ($\sim\text{Fe}(\text{OH})_3$), schwertmannite
553 ($\sim\text{FeO}(\text{OH})_{3/4}(\text{SO}_4)_{1/8}$), and e- Fe_2O_3 . Geochimica et Cosmochimica Acta, 68(5), 1049-
554 1059, doi:10.1016/S0016-7037(03)00371-5.
- 555 Majzlan, J., Stevens, R., Boerio-Goates, J., Woodfield, B.F., Navrotsky, A., Burns, P.C.,
556 Crawford, M.K., and Amos, T.G. (2004b) Thermodynamic properties, low-temperature heat-
557 capacity anomalies, and single-crystal X-ray refinement of hydronium jarosite,

- 558 (H₃O)Fe₃(SO₄)₂(OH)₆. *Physics and Chemistry of Minerals*, 31(8), 518-531,
559 doi:10.1007/s00269-004-0405-z.
- 560 Marion, G.M., Catling, D.C., and Kargel, J.S. (2003) Modeling aqueous ferrous iron chemistry at
561 low temperatures with application to Mars. *Geochimica et Cosmochimica Acta*, 67(22),
562 4251-4266, doi:10.1016/S0016-7037(03)00372-7.
- 563 Marion, G.M., Kargel, J.S., and Catling, D.C. (2008) Modeling ferrous-ferric iron chemistry with
564 application to Martian surface geochemistry. *Geochimica et Cosmochimica Acta*, 72(1), 242-
565 266, doi:10.1016/j.gca.2007.10.012.
- 566 Marion, G.M., Crowley, J.K., Thomson, B.J., Kargel, J.S., Bridges, N.T., Hook, S.J., Baldrige,
567 A., Brown, A.J., da Luz, B.R., and de Souza, C.R. (2009) Modeling aluminum-silicon
568 chemistries and application to Australian acidic playa lakes as analogues for Mars.
569 *Geochimica et Cosmochimica Acta*, 73(11), 3493-3511, doi:10.1016/j.gca.2009.03.013.
- 570 Marion, G.M., Catling, D.C., Zahnle, K.J., and Claire, M.W. (2010) Modeling aqueous perchlorate
571 chemistries with applications to Mars. *Icarus*, 207(2), 675-685,
572 doi:10.1016/j.icarus.2009.12.003.
- 573 McEwen, A.S., Eliason, E.M., Bergstrom, J.W., Bridges, N.T., Hansen, C.J., Delamere, W.A.,
574 Grant, J.A., Gulick, V.C., Herkenhoff, K.E., Keszthelyi, L., and others (2007) Mars
575 Reconnaissance Orbiter's High Resolution Imaging Science Experiment (HiRISE). *Journal of*
576 *Geophysical Research: Planets*, 112, E05S02, doi:10.1029/2005JE002605.
- 577 Milton, D.J., Barlow, B.C., Brett, R., Brown, A.R., Glikson, A.Y., Manwaring, E.A., Moss, F.J.,
578 Sedmik, E.C.E., Van Son, J., and Young, G.A. (1972) Gosses Bluff impact structure,
579 Australia. *Science*, 175, 4027, 1199-1207, doi:10.1126/science.175.4027.1199.

- 580 Morris, R.V., Golden, D.C., Bell, J.F. III, Lauer, H.V. Jr., and Adams, J.B. (1993) Pigmenting
581 agents in Martian soils: Inferences from spectral, Mössbauer, and magnetic properties of
582 nanophase and other iron oxides in Hawaiian palagonitic soil PN-9. *Geochimica et*
583 *Cosmochimica Acta*, 57, 4597-4609.
- 584 Morris, R.V., Klingelhöfer, G., Schröder, C., Rodionov, D.S., Yen, A., Ming, D.W., de Souza,
585 P.A., Wdowiak, T., Fleischer, I., Gellert, R., and others (2006) Mössbauer mineralogy of
586 rock, soil, and dust at Meridiani Planum, Mars: Opportunity's journey across sulfate-rich
587 outcrop, basaltic sand and dust, and hematite lag deposits. *Journal of Geophysical Research:*
588 *Planets*, 111, E12S15, doi:10.1029/2006JE002791.
- 589 Murchie, S.L., Arvidson, R., Bedini, P., Beisser, K., Bibring, J.-P., Bishop, J., Boldt, J., Cavender,
590 P., Choo, T., Clancy, R.T., and others (2007) CRISM (Compact Reconnaissance Imaging
591 Spectrometer for Mars) on MRO (Mars Reconnaissance Orbiter). *Journal of Geophysical*
592 *Research: Planets*, 112, E05S03, doi:10.1029/2006JE002682.
- 593 Osinski, G.R., and Spray, J.G. (2005) Tectonics of complex crater formation as revealed by the
594 Haughton impact structure, Devon Island, Canadian High Arctic, *Meteoritics and Planetary*
595 *Science*, 40, 12, 1813-1834, doi:10.1111/j.1945-5100.2005.tb00148.x.
- 596 Osinski, G.R., and Pierazzo, E. (2012) *Impact Cratering: Processes and Products*, 330 p. Wiley-
597 Blackwell, Hoboken, New Jersey.
- 598 Post, J.E. (1999) Manganese oxide minerals: Crystal structures and economic and environmental
599 significance. *Proc. Natl. Acad. Sci. USA*, 96, 3447-3454, doi:10.1073/pnas.96.7.3447.

- 600 Poulet, F., Bibring, J.-P., Mustard, J.F., Gendrin, A., Mangold, N., Langevin, Y., Arvidson, R.E.,
601 Gondet, B., Gomez, C., Berthé, M., and others (2005) Phyllosilicates on Mars and
602 implications for early Martian climate. *Nature*, 438, 623-627, doi:10.1038/nature04274.
- 603 Rice, M.S., Bell, J.F. III, Cloutis, E.A., Wang, A., Ruff, S.W., Craig, M.A., Bailey, D.T., Johnson,
604 J.R., de Souza Jr., P.A., and Farrand, W.H. (2010) Silica-rich deposits and hydrated minerals
605 at Gusev Crater, Mars: Vis-NIR spectral characterization and regional mapping. *Icarus*, 205,
606 375-395, doi:10.1016/j.icarus.2009.03.035.
- 607 Sherman, D.M. (1984) The electronic structures of manganese oxide minerals. *American*
608 *Mineralogist*, 69, 788-799.
- 609 Squyres, S.W., Arvidson, R.E., Baumgartner, E.T., Bell, J.F., Christensen, P.R., Gorevan, S.,
610 Herkenhoff, K.E., Klingelhöfer, G., Madsen, M.B., Morris, R.V., and others (2003) Athena
611 Mars rover science investigation. *Journal of Geophysical Research: Planets*, 108, 8062,
612 doi:10.1029/2003JE002121, E12.
- 613 Squyres, S.W., Arvidson, R.E., Bell, J.F., Calef, F., Clark, B.C., Cohen, B.A., Crumpler, L.A.,
614 Souza, P.A. de, Farrand, W.H., Gellert, R., and others (2012) Ancient impact and aqueous
615 processes at Endeavour crater, Mars. *Science*, 336, 570-576, doi:10.1126/science.1220476.
- 616 Stöffler, D., Artemieva, N.A., Wunnemann, K., Reimold, W.U., Jacob, J., Hansen, B.K., and
617 Summerson, I.A.T. (2013) Ries crater and suevite revisited-observations and modeling, Part
618 I: observations. *Meteoritics & Planetary Science*, 48, 515-589, doi:10.1111/maps.12086.
- 619 Tosca, N.J., McLennan, S.M., Clark, B.C., Grotzinger, J.P., Hurowitz, J.A., Knoll, A.H., Schroder,
620 C., and Squyres, S.W. (2005) Geochemical modeling of evaporation processes on Mars:
621 Insight from the sedimentary record at Meridiani Planum. *Earth and Planetary Science*
622 *Letters*, 240(1), 122-148, doi:10.1016/j.epsl.2005.09.042.

- 623 Tosca, N.J., Smirnov, A., and McLennan, S.M. (2007) Application of the Pitzer ion interaction
624 model to isopiestic data for the $\text{Fe}_2(\text{SO}_4)_3\text{-H}_2\text{SO}_4\text{-H}_2\text{O}$ system at 298.15 and 323.15 K.
625 *Geochimica et Cosmochimica Acta*, 71(11), 2680-2698, doi:10.1016/j.gca.2007.03.020.
626
- 627 VanBommel, S.J., Gellert, R., Berger, J.A., Campbell, J.L., Thompson, L.M., Edgett, K.S.,
628 McBride, M.J., Minitti, M.E., Pradler, I., Boyd, N.I. (2016) Deconvolution of distinct
629 lithology chemistry through oversampling with the Mars Science Laboratory Alpha Particle
630 X-ray Spectrometer. *Journal of X-ray Spectrometry*, (Accepted).
- 631 Vaughan, D.J., and Rosso, K.M. (2006) Chemical bonding in sulfide minerals. *Reviews in*
632 *Mineralogy and Geochemistry*, 61, 231-264.
- 633 Wolters, F., Lagaly, G., Nueesch, R., and Emmerich, K. (2009) A comprehensive
634 characterization of dioctahedral smectites. *Clays and Clay Minerals*, 57, 115-133,
635 doi:10.1346/CCMN.2009.0570111.
636

Figure Captions

637
638

639 **Figure 1.** HiRISE-based mosaic showing Endeavour Crater, Opportunity's traverses, and key
640 locations on the crater rim explored by the rover. Endeavour is largely buried by later Burns
641 formation sulfate-rich sandstones and thus only high portions of the crater rim are exposed. Box
642 shows the location of the portion of the mosaic shown in Fig. 2.

643 **Figure 2.** HiRISE-based image showing Botany Bay and Murray Ridge, with Opportunity's
644 traverses shown. Cook Haven is a gentle swale on the Murray Ridge rim segment and was the site
645 for Opportunity's sixth winter sojourn. Bristol Well is a Ca sulfate vein and Tuscaloosa is a
646 breccia outcrop examined by Opportunity, and both are shown to provide context for the rover's
647 exploration of Murray Ridge. Box A is the location shown in Fig. 3 that illustrates concentric and
648 radial fractures in the Burns formation. Box B is the location shown in Fig 4 that shows fractures
649 and the northern portion of Murray Ridge. HiRISE image ESP_036753_1775_MRGB (merged
650 color and gray scale).

651 **Figure 3.** Portion of the HiRISE-based image segment covering Botany Bay, highlighting the
652 locations of concentric fractures that are interpreted to have propagated up through the Burns
653 formation outcrops just above a buried portion of Endeavour's rim between the Cape York and
654 Murray Ridge rim segments. Radial fractures are evident extending to the east and northeast into
655 Endeavour. HiRISE image ESP_036753_1775_MRGB.

656 **Figure 4.** Portion of the HiRISE-based image segment covering the northern part of Murray
657 Ridge. Concentric fractures are evident extending into the Burns formation outcrops located to the
658 north of Murray Ridge. Note the radial fracture (strike N85°W) extending from the west to the
659 east, terminating near the Cook Haven location. Spinifex and Moreton Island are two of

660 Opportunity's breccia outcrop targets and are shown for context. HiRISE image
661 ESP_036753_1775_MRGB.

662 **Figure 5.** Pancam false color image mosaic of the Moreton Island outcrop on Murray Ridge, with
663 the Tangalooma and Mount Tempest in-situ targets shown. These highly fractured rocks are
664 impact breccias with embedded rock clasts. For reference the outcrop with the two in-situ targets
665 is approximately 0.25 m wide. Pancam images were acquired on sols 3494-3496, with bands
666 centered at 0.753, 0.535, and 0.432 μm shown as RGB colors. This band assignment is the same as
667 other Pancam false color data shown in subsequent figures. Mosaic available as
668 <http://photojournal.jpl.nasa.gov/catalog/PIA17753>.

669 **Figure 6.** Navcam image mosaic acquired on sol 3512 while Opportunity was south of Cook
670 Haven before entering this gentle swale for its winter campaign. View is to the northeast and
671 provides an overview of the polygonally fractured, low relief outcrops that dominate Cook Haven.
672 Two prominent fractures are shown that intersect at right angles, with strikes of N75°E and
673 N10°W. Green Island is an in-situ target for which Microscopic Imager (MI) and Alpha Particle
674 X-ray Spectrometer (APXS) data were acquired after brushing using the Rock Abrasion Tool
675 (RAT). For reference the Green Island outcrop is ~0.35 m wide. A dust devil can be seen on the
676 floor of Endeavour Crater. Navcam mosaic 1NNZ12ILFCACYPDPP0673L000M2.

677 **Figure 7** Orthorectified view of Navcam image mosaic shown in Fig. 6, augmented with a
678 portion from a later Navcam mosaic (Site 182, position 194, sol 3507, where site is a location
679 where the rover coordinate system is set to zero, and position is a location relative to that new
680 coordinate system) to show terrain elements masked by the rover in the earlier data. The two
681 orthogonal fractures labeled in Fig. 6 are shown, along with the soil-filled fracture (N80°W strike,
682 similar in azimuth to the inferred fracture extending into Cook Haven from the west, Fig. 4) from

683 which Opportunity excavated Pinnacle and Stuart Island rocks. The rover's turn in place and drive
684 into Cook Haven is evident from tracks on lower left of the figure. Navcam data from site 182,
685 position 194 are from a mosaic acquired on sol 3507, and the product ID is
686 1NNZ07ILFCAVRTCMP1797L000M2. Navcam data from site 182, position 233 are shown in
687 Fig. 5 in cylindrical projection whereas the orthorectified view for this figure is derived from
688 product ID 1NNZ12ILFCAVRTDPP0673L000M2.

689 **Figure 8.** Pancam false color image mosaic acquired on sol 3567 from Cook Haven looking south
690 after excavating Pinnacle and Stuart Island rocks. Also shown are in-situ bedrock targets Cape
691 Darby and Cape Elizabeth. Anchor Point in-situ targets are soils excavated from the soil-filled
692 fracture (N80°W strike), King Island is another target with a bright coating and perhaps the mate
693 of Pinnacle Island, and Sledge Island may or may not have existed as an erratic rock before
694 Opportunity arrived. Mosaic product IDs 1PPZ67ILFCACYLFCP2397L222M1,
695 1PPZ67ILFCACYLFCP2397L555M1, and 1PPZ67ILFCACYLFCP2397L777M1 were used to
696 generate the false color mosaic. For reference Pinnacle Island is ~3.5 cm wide and Stuart Island is
697 ~12 cm in its longest dimension.

698 **Figure 9.** Pancam false color image of Green Island, a brushed in-situ target. The brushed circle is
699 ~3.8 cm in diameter and is dark as compared to surrounding bedrock because wind-blown dust
700 and sand have been removed. A small rock clast can be seen embedded in the fine-grained matrix
701 of the breccia. The central reddish spot is remnant dust and soil from the brushing activity. Soil-
702 filled fractures are evident on the right side of the image. Generated from Product IDs
703 1P445203637RADCAG7P2537L2C1, 1P445203721RADCAG7P2537L5C1, and
704 1P445203794RADCAG7P2537L7C1.

705 **Figure 10.** Pancam false color images of impact breccias in the Bristol Well in-situ target location
706 on Murray Ridge. Note the relatively large embedded rock clasts as compared to Green Island in
707 Cook Haven. The **right**-hand view shows the location of the Bristol Well in-situ target for which
708 three overlapping in-situ observations were acquired. This target is located to the south of the area
709 covered by the Pancam data shown in the **left**-hand view. Table 1 shows that the compositions are
710 consistent with the dominance of Ca-sulfate veins. For reference the large breccia block on the
711 lower left side of the **left** image is ~0.35 m high. Portion of Pancam mosaic product IDs
712 1PPAG3ILFCDCYLAHP2277L222M, 1PPAG3ILFCDCYLAHP2277L555M1, and
713 1PPAG3ILFCDCYLAHP2277L777M1 were used to generate the **left**-hand image. Pancam
714 product IDs 1P453282110RADCDAAP2586L2C1, 1P453282143RADCDAAP2586L5C1, and
715 1P453282180RADCDAAP2586L7C1 were used to generate the **right**-hand image.

716 **Figure 11.** Portion of a Front Hazcam image is shown on the **left** for the Sarcobatus in-situ targets
717 for a rock clast (two overlapping measurements) and the brushed matrix target (Sarcobatus_flat).
718 Pancam false color image of the targets is shown on the **right**. For reference the brushed spot is
719 ~3.8 cm wide. Hazcam product ID 1F454088547FFLCDBAP1148R0M1. Pancam product IDs
720 1P454529822RADCDBAP2589L2C1, 1P454529907RADCDBAP2589L5C1, and
721 1P454529979RADCDBAP2589L7C1.

722 **Figure 12.** Ternary plot of mole fraction Al_2O_3 –(CaO+Na₂O+K₂O)–(FeO_T+MgO) with
723 Shoemaker and Matijevic formation data plotted for Cape York, along with Murray Ridge
724 observations, and various phyllosilicates and pyroxene compositions. Espérance is a suite of in-
725 situ targets within a Matijevic formation fracture in which deeper grinding using the RAT and
726 APXS observations showed a trend to montmorillonite. The Murray Ridge data lie within the field
727 of basalts, with no evidence for alteration to phyllosilicate compositions. Montmorillonite data are
728 from Emmerich et al. (2009) and Wolters et al. (2009).

729 **Figure 13.** Scatter plot of S and Cl contents for APXS measurements acquired on Murray Ridge.
730 Cook Haven data are shown in italics. Pinnacle and Stuart Island (PI and SI, respectively)
731 measurements show large enrichments in S, with increased Cl for PI as opposed to SI
732 measurements. The main trend shows that Cook Haven outcrops (CD, Cape Darby; CE, Cape
733 Elizabeth, TAA, Turn Again Arm; GI_b, Green Island, brushed) are enriched in S and Cl as
734 compared to other Murray Ridge targets. AP, Anchor Point, delineates a pair of measurements on
735 soils dislodged by Opportunity, along with PI and SI rocks. Augustine is a rock just south of Cook
736 Haven. Bristol Well corresponds to three measurements across a C sulfate vein. Sarcobatus_clast
737 and Sarcobatus_flat_b (brushed) are targets to the south of Cook Haven. The latter is a breccia
738 matrix enriched in Cl.

739 **Figure 14.** Pancam false color image acquired on sol 3541 in which the brightness has been
740 combined with an MI mosaic of Pinnacle Island. The locations of dark and bright coatings are
741 shown, along with dusty and fresh rock. The box shows the location of an MI-based stereo
742 anaglyph shown in Fig. 15, and the circles represent ~100% fields of view and locations for the
743 five overlapping APXS observations. For reference Pinnacle Island is ~3.5 cm wide. Pancam
744 product IDs 1P442541197RADCAEOP2595L2C1, 1P442541258RADCAEOP2595L5C1, and
745 1P442541300RADCAEOP2595L7C1. MI product ID 1M442544805IFFCAEOP2955M2F1.

746 **Figure 15.** MI-based anaglyph from overlapping stereo coverage is shown for a portion of
747 Pinnacle Island. The coating can be seen directly on top of the rock, with the dark coating
748 occupying the center of the rock and interpreted to overlie the bright coating. The dark coating
749 exhibits a lumpy or popcorn structure. MI product ID 1M442544805IFFCAEOP2955M2F1 and
750 four other MI images were used to construct the anaglyph. Illumination is from the top of the
751 scene.

752 **Figure 16.** Pancam false color image of Stuart Island acquired on sol 3567 showing the locations
753 and 100% field of view of the four APXS observations. Box delineates location for the MI-based
754 anaglyph shown in Fig. 17. The location is denoted from which a dark area spectrum derived from
755 Pancam data is shown in Fig. 18. For reference Stuart Island is about 0.12 m in its long dimension.
756 Pancam product IDs 1P445650967RADCAGYP2539L2C1,
757 1P445651052RADCAGYP2539L5C1, and 1P445651127RADCAGYP2539L7C1.

758 **Figure 17.** MI-based anaglyph of a portion of Stuart Island that shows a thin bright annulus
759 around what is interpreted to be a rock clast. This bright annulus is surrounded by a dark coating.
760 A second clast is surrounded by a dark coating. MI product ID
761 1M445651708IFFCAGYP2935M2F1 and four other MI frames were used to construct the
762 anaglyph. Target was fully shadowed when the data were acquired.

763 **Figure 18.** Locations of Pancam spectral endmembers derived from the unmixing algorithm are
764 shown on the Pancam false color image on the **left**, and mean spectra for these regions are shown
765 on the **right**. Also shown is the mean spectrum for the dark area on Stuart Island. One standard
766 deviation error bars are also plotted. The dark coating spectra for the Island rocks are
767 indistinguishable and unique for any Pancam observation. The spectra lack the ferric absorption
768 edge shortward of $\sim 0.7 \mu\text{m}$ that is characteristic of Martian spectra, and evident for the other three
769 spectra shown in the figure. The dusty rock spectrum has the deepest ferric absorption edge,
770 followed by the bright coating spectrum, and the rock spectrum has the shallowest absorption.

771 **Figure 19.** Pinnacle Island endmember concentration maps for dark and bright coatings, fresh
772 rock, and dusty rock are shown, along with APXS fields of view that correspond to the highest
773 retrieved areal concentrations of each of these endmembers (Table 3). As discussed in the text the
774 dusty and fresh rock endmembers were combined to a single rock endmember in the retrievals.

775 **Figure 20.** Correspondence analysis for the first two factor loadings is shown for Murray Ridge
776 observations, except for the three Bristol Well Ca sulfate vein measurements. Also included in the
777 calculations were the three Pinnacle Island-based endmembers (rock, dark coating, and bright
778 coating), which on the plot extend beyond, but encapsulate the data. The endmembers show the
779 affinity of the dark coating for Mn, S, P, and Ca whereas the bright coating endmember shows an
780 affinity for Mg and S.

781 **Figure 21.** Bivariate plots are shown of SiO₂, MgO, MnO as a function of SO₃ contents, along
782 with CaO as a function of P₂O₅, for Cook Haven APXS measurements. Bright and dark coatings
783 and rock retrieved endmember compositions are also shown. Error bars are plotted for the bright
784 coating (Table 2). For the other two endmembers the errors are comparable to the box symbol
785 sizes. Least squares linear fits to the APXS data (not endmembers) are shown as straight lines,
786 along with the square of the Pearson linear correlation coefficient. These bivariate plots were
787 chosen to illustrate trends with high correlation coefficients, based on results from the
788 correspondence analysis shown in Fig. 20.

789 **Figure 22.** MnO vs. Ni bivariate plot is shown for Cook Haven outcrops, Anchor Point soils, and
790 Pinnacle and Stuart Islands. Least squares linear fits to the data are shown as straight lines, along
791 with the square of the Pearson linear correlation coefficient.

792 **Figure 23** The Pinnacle Island dark coating endmember spectrum is shown, together with data
793 from the region with the highest concentration of this endmember mapped to Stuart Island. Data
794 are also shown for lab spectra of synthesized Mn oxides. Mg and Mn-bearing sulfates have much
795 brighter spectra as shown by the labels and arrows at the top of the plot. Only high valence state
796 Mn oxides are compatible with the spectral trends observed in the dark areas on the two Island
797 rocks and the compositions of these two targets. A unique mineral phase is impossible to retrieve,

798 given the number of unknowns (optical constants, grain size and shape of each constituent,
799 together with coating porosity) involved in any retrievals, together with the limited Pancam
800 spectral range and number of bands.

801 **Figure 24.** Mass fractions of minerals produced by equilibrating the endmember coating
802 compositions (Table 2) with water in a geochemical reaction model. The “Other Salts/Oxides”
803 category contains rutile and an array of minor sulfate and chloride salts.

804 **Figure 25.** Fe and Mn concentrations are plotted for all of Opportunity’s APXS observations
805 through Murray Ridge, together with the three endmember values retrieved from Pinnacle Island
806 data. The trends for the Island rocks are unique and indicate a special process that concentrated
807 Mn relative to Fe in the bright and, especially, the dark coatings.

808 **Figure 26.** Ternary plot for all Meridiani Planum and Endeavour Crater soil and bedrock APXS
809 analyses through measurements acquired on Murray Ridge and calculated to $\text{SO}_3 = \text{Cl} = 0.0$
810 weight percent. The trends show the unique chemistry of Pinnacle and Stuart Island targets as
811 compared to other rock and soil compositions and are broadly consistent with precipitation from
812 aqueous sulfate solutions. The dashed arrow terminates on the extrapolated SO_3 -free composition
813 of the mixed-cation sulfate-dominated endmember, which is also the location of the predicted dark
814 coating endmember. The rock endmember plots within the rock and soil field whereas the bright
815 coating endmember plots between the other two endmembers, slightly displaced toward the Fe
816 apex. This trend is consistent with the ferric edge observed in the spectrum for this endmember
817 and the inferred presence of one of more Fe^{3+} -bearing phases. North Pole_2 is a dust-covered soil
818 target measured by Opportunity on the Cape York rim segment of Endeavour Crater. This target
819 has a composition that is representative of Martian global dust and plots near the center of the
820 cluster.

822

Tables

823

824 **Table 1.** APXS compositional data for the western portion of Murray Ridge, including Cook
825 Haven localities for key measurements discussed in this paper. Values are oxide concentrations
826 unless otherwise indicated. Also given in the table are the average percentage uncertainty for each
827 element representing the statistical error for each measured spot (Gellert et al. 2006). These are
828 typically better for higher abundances and worse for lower. The last column gives the average
829 relative accuracy for each element found for the MER APXS calibration with homogeneous
830 powdered geological reference samples (Gellert et al. 2006).

Sol	3463	3498	3502	3522	3535	3542	3546	3548	3551	3560	3564
Type ^a	RB	RU	RU	RU	RU	RB	RU	RU	RU	RU	RU
Target	Spinifex	Tanga- looma	Mount Tempest	Cape Darby	Cape Darby 2	Cape Elizabeth	Pinnacle Island	Pinnacle Island 2	Pinnacle Island 3	Pinnacle Island 4	Pinnacle Island 5
Norm	76	68	72	66	73	74	31	39	41	28	40
SiO ₂	45.7	45.7	46.3	46.3	45.5	44.7	28.1	23.8	18.1	36.2	20.1
TiO ₂	1.04	1.09	1.16	1.13	1.18	0.96	0.76	0.62	0.44	0.91	0.58
Al ₂ O ₃	8.76	9.43	10.30	9.39	9.23	9.06	5.75	4.70	3.48	7.57	3.68
Cr ₂ O ₃	0.22	0.20	0.21	0.25	0.27	0.20	0.21	0.12	0.10	0.22	0.10
FeO _T ^b	17.6	16.2	16.1	17.0	17.1	16.7	16.6	16.0	15.1	17.9	15.5
MnO _T ^b	0.78	0.36	0.40	0.31	0.35	0.26	1.67	2.12	3.48	1.30	3.35
MgO	8.85	8.58	7.48	6.96	7.13	8.01	12.06	13.26	13.00	9.43	11.50
CaO	6.18	6.29	7.14	6.67	6.47	5.92	5.45	6.08	7.66	5.69	8.26
Na ₂ O	2.32	2.04	2.39	2.25	2.37	2.54	1.01	1.02	0.86	1.57	0.84
K ₂ O	0.70	0.23	0.30	0.46	0.49	0.36	0.32	0.17	0.14	0.41	0.13
P ₂ O ₅	1.18	1.15	1.18	0.97	0.98	0.89	1.57	2.18	2.37	1.33	2.44
SO ₃	5.52	7.82	6.25	7.20	7.66	9.17	25.44	28.81	34.51	16.44	32.70
Cl	0.95	0.74	0.75	1.06	1.17	1.12	0.92	0.95	0.66	0.91	0.65
Ni	537	523	342	394	394	447	661	884	1001	354	736
(ppm)											
Zn	460	118	87	258	203	121	185	130	155	204	116
(ppm)											
Br	706	97	43	112	110	78	262	476	334	144	269
(ppm)											
Sol	3569	3573	3574	3575	3577	3581	3583	3587	3598	3664	3666
Type ^a	RB	RU	RU	RU	RU	SD	SD	RU	RB	RU	RU
Target	Green Island	Stuart Island 1	Stuart Island 2	Stuart Island 3	Stuart Island 4	Anchor Point 1	Anchor Point 2	Sledge Island 1	Turnagain Arm	Bristol Well 1	Bristol Well 2
Norm	78	75	82	65	73	59	78	63	76	66	66
SiO ₂	43.3	27.3	22.5	16.1	25.6	37.8	39.3	47.6	44.5	42.8	41.9
TiO ₂	1.02	0.78	0.65	0.57	0.65	0.95	1.07	0.63	1.04	0.94	0.92
Al ₂ O ₃	8.89	5.67	4.38	3.60	4.87	7.00	7.86	10.44	9.10	8.50	8.25
Cr ₂ O ₃	0.19	0.13	0.17	0.14	0.16	0.35	0.38	0.21	0.20	0.27	0.26
FeO _T ^b	16.7	16.2	16.5	17.0	16.8	18.2	18.3	12.8	16.4	15.1	14.8
MnO _T ^b	0.27	1.57	2.01	2.85	3.37	0.75	1.01	0.30	0.28	0.34	0.33
MgO	7.31	12.31	14.49	15.58	11.65	8.14	8.52	6.35	8.05	6.98	6.86
CaO	6.38	5.36	3.75	4.05	4.85	7.28	7.07	9.65	5.98	9.42	10.00

Na ₂ O	2.53	0.93	0.82	0.53	0.86	1.74	1.92	2.48	2.32	2.15	2.03
K ₂ O	0.37	0.18	0.12	0.09	0.28	0.33	0.35	0.28	0.36	0.49	0.45
P ₂ O ₅	0.99	1.08	0.91	0.98	1.40	1.82	1.53	0.82	0.95	1.01	1.06
SO ₃	10.48	28.20	33.31	38.21	28.95	15.09	12.06	7.74	9.37	11.00	12.04
Cl	1.54	0.22	0.26	0.21	0.33	0.43	0.45	0.65	1.36	0.95	0.97
Ni (ppm)	376	547	715	1024	1022	372	603	123	453	312	269
Zn (ppm)	152	82	111	175	231	218	198	138	114	321	302
Br (ppm)	65	40	88	77	77	117	180	94	167	75	81

Sol Type ^a	3667	3671	3675	3676	3707	3708	3709	Avg. Stat.	Approx. Accuracy
Target	Bristol Well 3	Sarcobatus Flat 1	Sarcobatus Sarcobatus Clast	Sarcobatus Sarcobatus Clast 2	Sodaville	Tuscaloosa	Sodaville 2	Error (%)	Accuracy (%)
Norm	50	76	37	41	65	73	47		
SiO ₂	45.4	44.9	46.0	46.2	45.4	45.9	45.6	2	4
TiO ₂	1.15	0.98	1.15	1.41	1.11	1.05	1.12	10	20
Al ₂ O ₃	8.89	8.84	9.89	11.23	9.18	9.10	9.25	2	7
Cr ₂ O ₃	0.27	0.23	0.20	0.14	0.28	0.19	0.24	25	20
FeO _T ^b	17.6	17.6	16.5	15.3	18.0	17.1	17.7	2	10
MnO _T ^b	0.36	0.24	0.51	0.27	0.25	0.14	0.23	10	10
MgO	7.14	7.78	6.98	6.21	7.42	8.20	7.34	3	15
CaO	7.17	6.38	7.72	8.17	6.56	6.20	6.75	2	7
Na ₂ O	2.03	2.30	1.90	2.00	2.29	2.13	2.22	15	15
K ₂ O	0.50	0.48	0.51	0.44	0.55	0.41	0.52	10	15
P ₂ O ₅	1.00	1.17	1.09	1.61	1.01	1.11	1.07	10	15
SO ₃	7.36	7.10	6.40	6.12	6.69	7.18	6.56	2	15
Cl	1.05	1.92	1.06	0.83	1.12	1.19	1.24	4	30
Ni (ppm)	365	293	193	292	391	371	305	15	15
Zn (ppm)	361	162	295	151	372	132	325	10	15
Br (ppm)	102	98	69	69	71	117	87	10	20

831 Notes: ^aAbbreviations for Type: RU = rock, unbrushed; RB = rock, brushed; SD = soil, disturbed. ^bTotal Fe reported
832 as FeO (FeO_T) and Mn as MnO_T.

833

834 **Table 2.** Compositions and associated errors for Pinnacle Island endmembers in weight percent
 835 for each oxide.

	Abundance (wt%)			Error (wt%)		
	Dark	Bright	Rock	Dark	Bright	Rock
SiO ₂	0.42	27.03	47.90	1.25	10.80	0.86
TiO ₂	0.07	0.83	1.15	0.10	0.25	0.03
Al ₂ O ₃	0.00	5.48	9.66	0.00	2.12	0.01
Cr ₂ O ₃	0.00	0.22	0.28	0.02	0.08	0.01
FeO	14.64	17.64	17.35	0.73	0.99	0.22
MnO	5.41	1.38	0.00	0.18	1.39	0.06
MgO	16.5	14.26	6.60	0.61	1.83	0.16
CaO	7.89	2.11	6.62	0.70	1.53	0.30
Na ₂ O	0.00	0.71	2.46	0.00	0.43	0.06
K ₂ O	0.00	0.15	0.46	0.00	0.07	0.01
P ₂ O ₅	3.27	0.00	1.07	0.31	0.49	0.12
SO ₃	51.42	30.07	5.15	2.06	10.14	1.02
Cl	0.31	0.00	1.23	0.29	0.10	0.08
Ni	767	941	407	883	739	159
Zn	0	177	216	28	116	38
Br	14	74	206	178	81	51

836

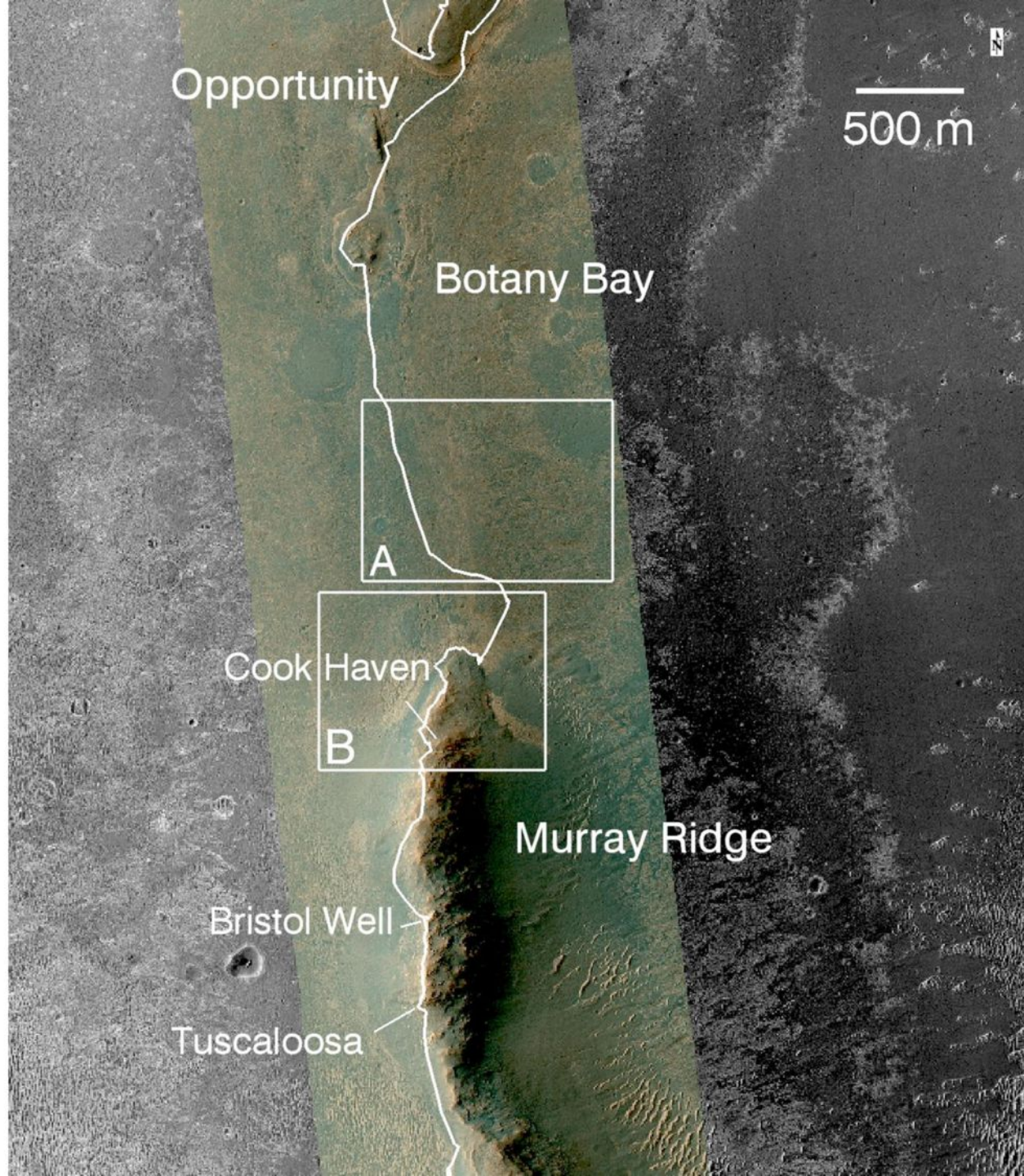
837

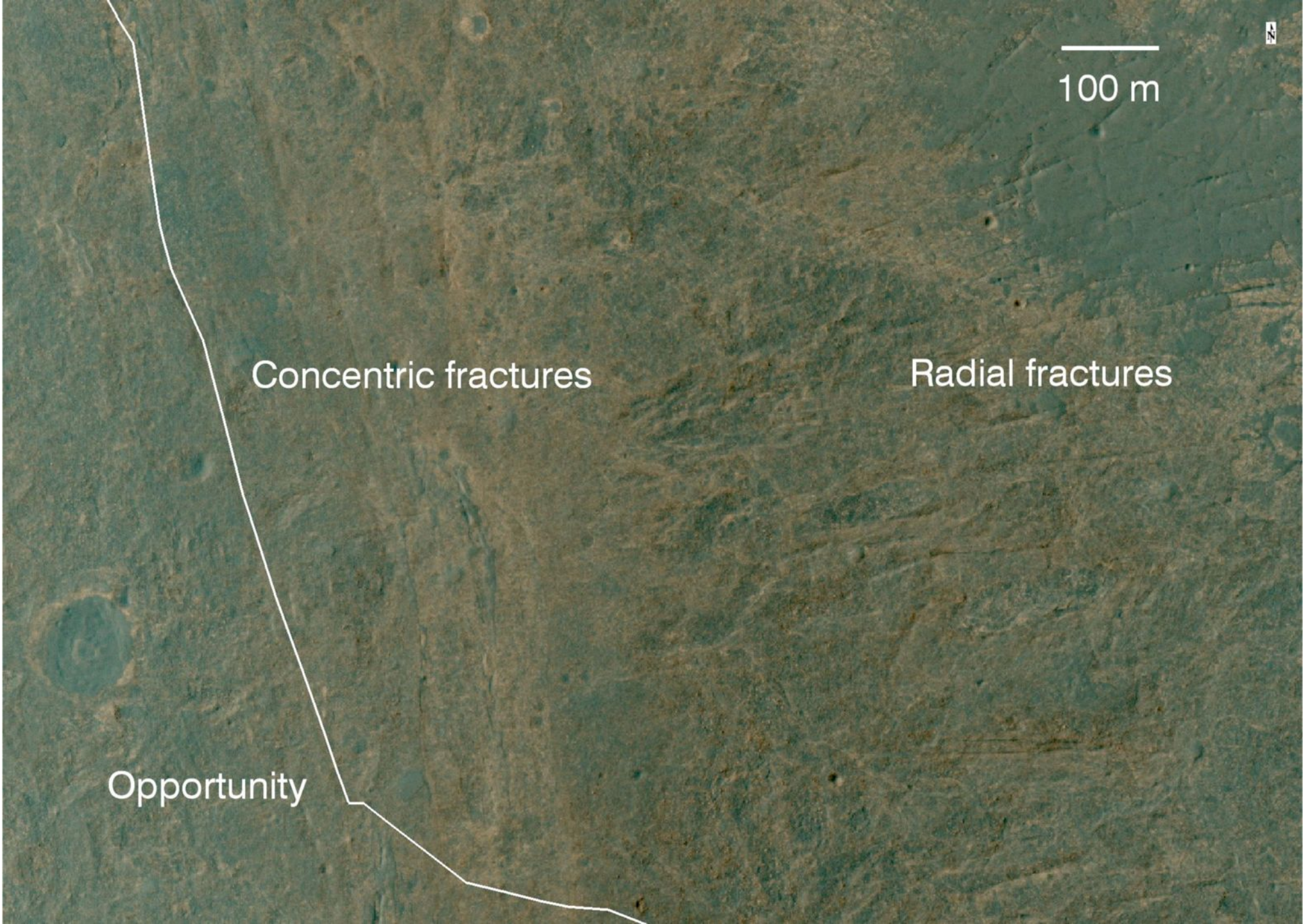
838 **Table 3.** Endmember abundances for APXS observations, with numbers in percent for each
 839 endmember and estimated errors.

	Abundance (%)			Error (%)		
	Dark	Bright	Rock	Dark	Bright	Rock
CapeDarby	4	2	94	4	5	3
CapeDarby2	5	2	93	5	6	3
CapeElizabeth	5	7	88	5	9	6
PinnacleIsland1	38	9	53	3	1	3
PinnacleIsland2	40	11	50	3	3	1
PinnacleIsland3	56	5	38	2	2	1
PinnacleIsland4	23	5	72	2	1	2
PinnacleIsland5	64	1	35	5	2	6
GreenIsland	4	8	88	4	12	7
StuartIsland1	22	49	29	14	15	11
StuartIsland2	22	69	9	22	15	12
StuartIsland3	40	58	2	22	16	6
StuartIsland4	34	41	25	12	11	10
AnchorPoint1	13	17	70	7	16	9
AnchorPoint2	12	14	74	12	24	12
TurnagainArm	3	10	87	4	9	6

840







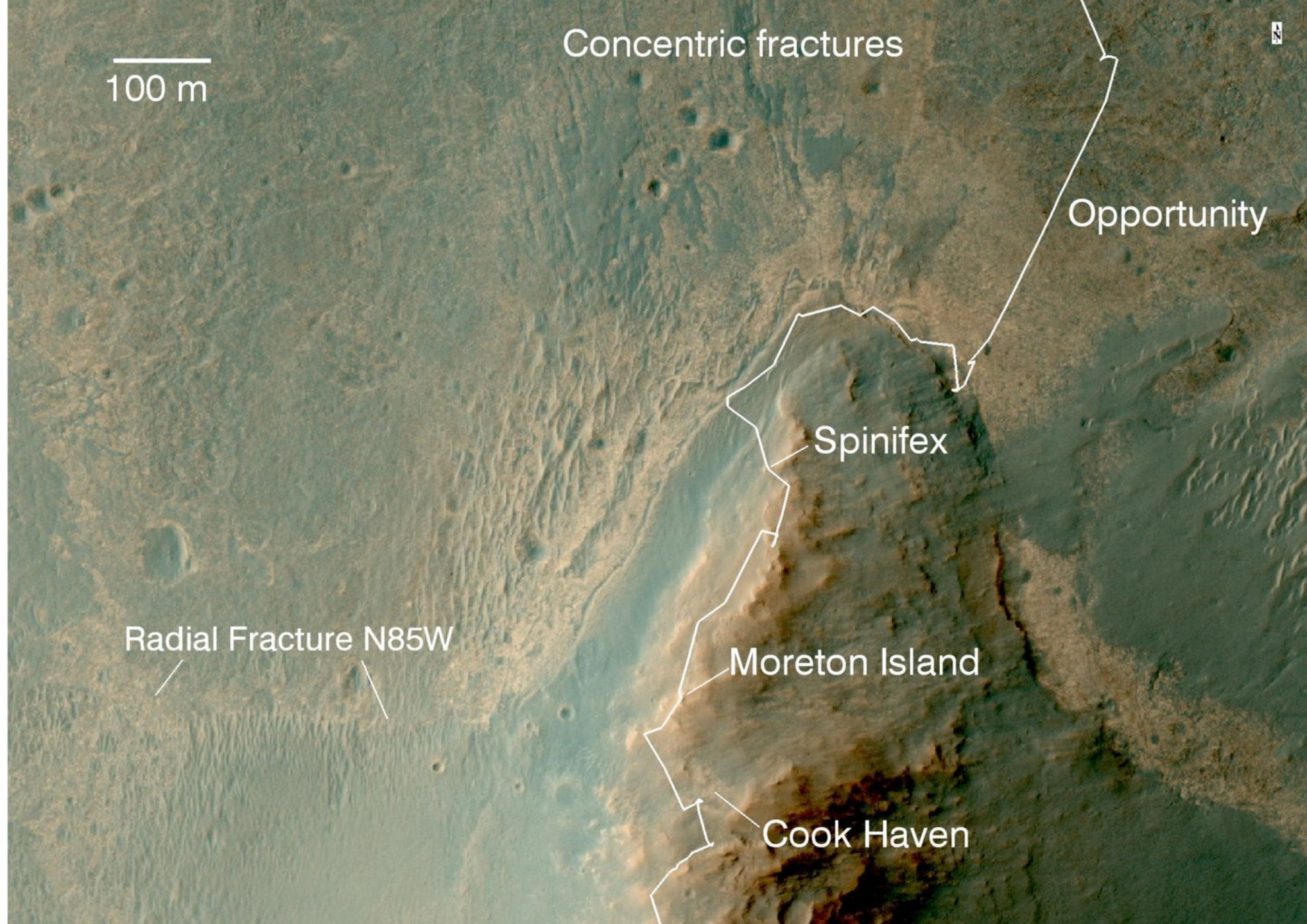
Opportunity

Concentric fractures

Radial fractures

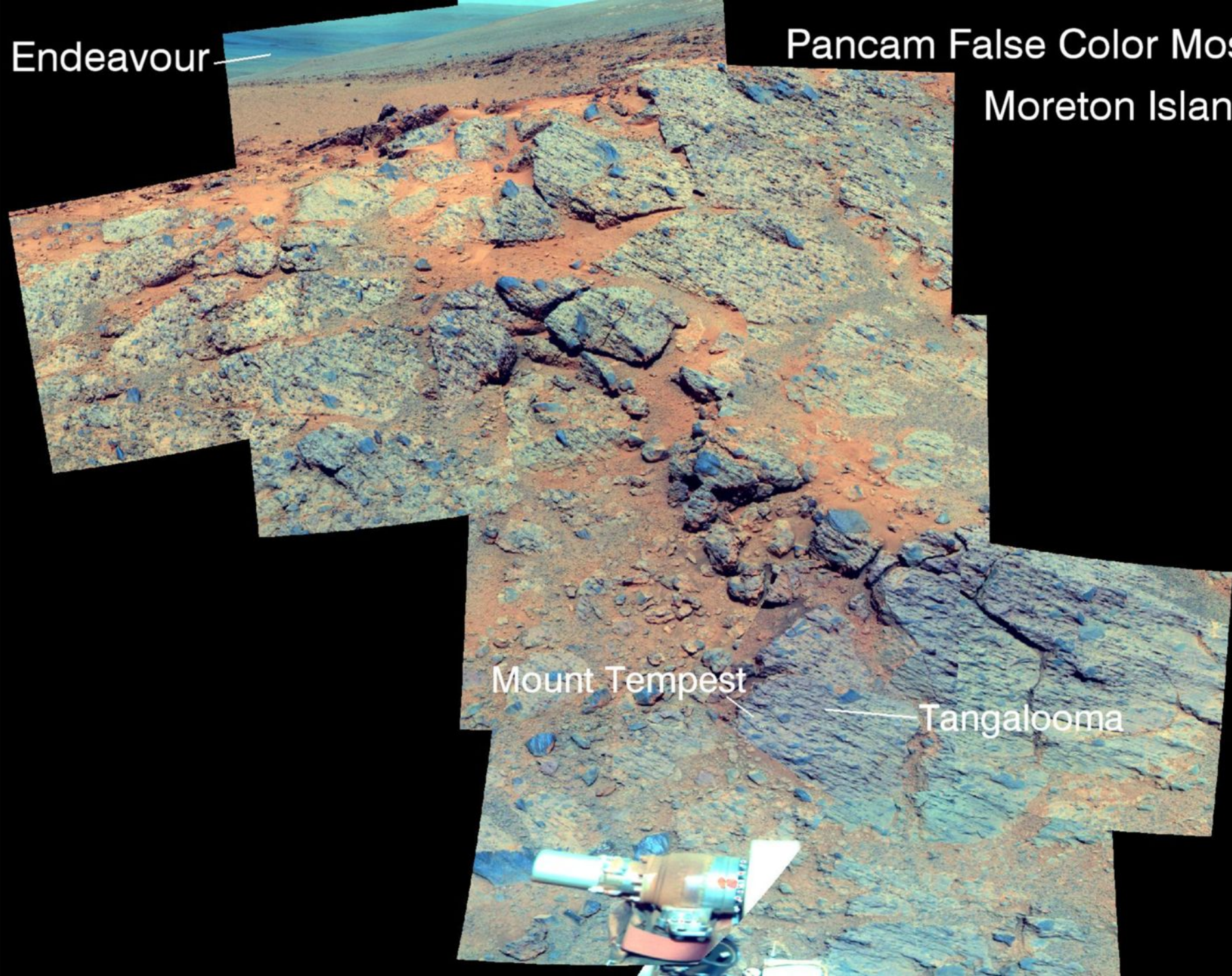
100 m





Endeavour

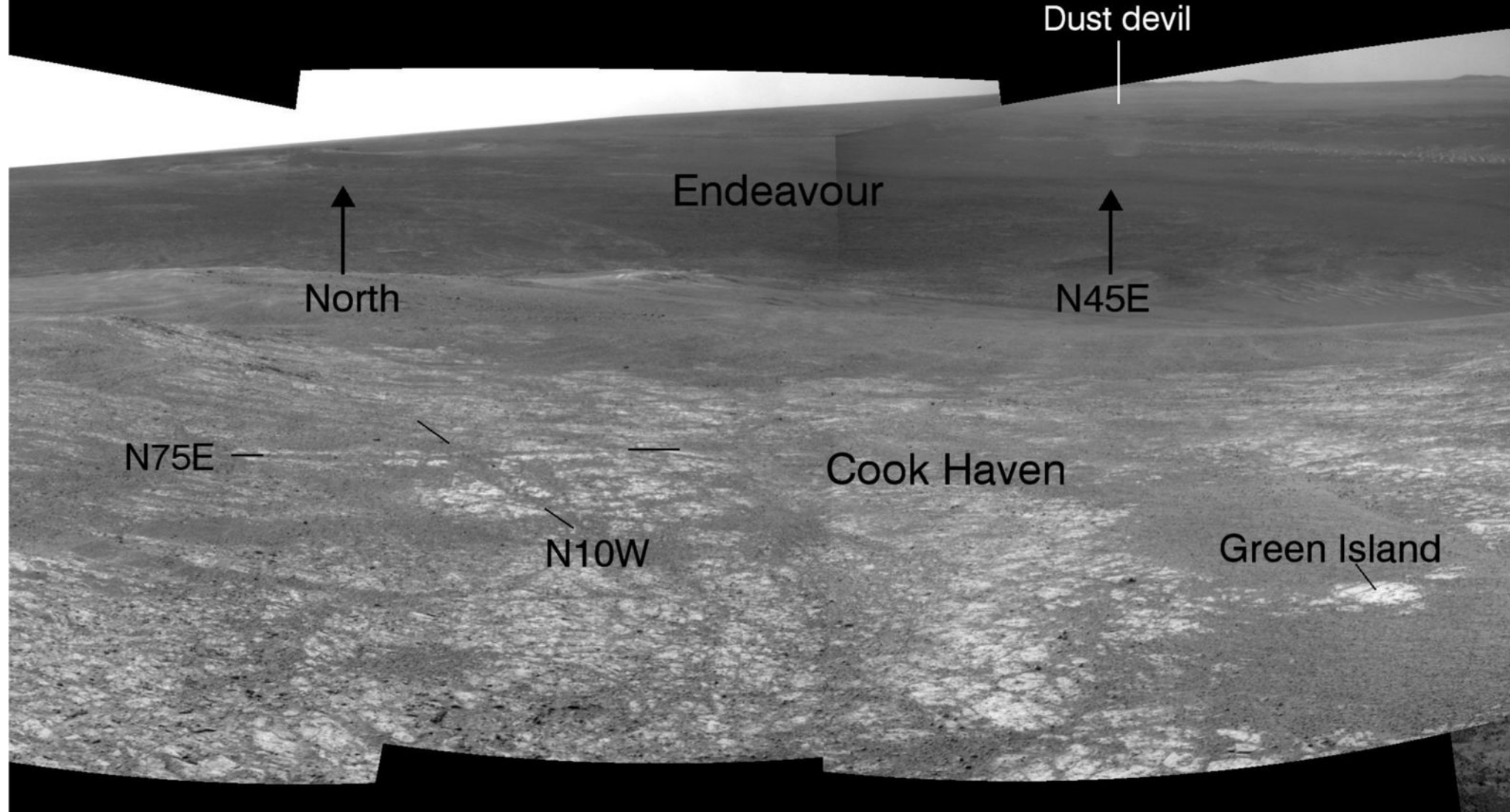
Pancam False Color Mosaic
Moreton Island



Mount Tempest

Tangalooma

Navcam Mosaic Cook Haven



Navcam Overhead Mosaic Cook Haven

Site 182, pos 233

↑
North
1.5 m

N75E →

↑
N10W

Green Island

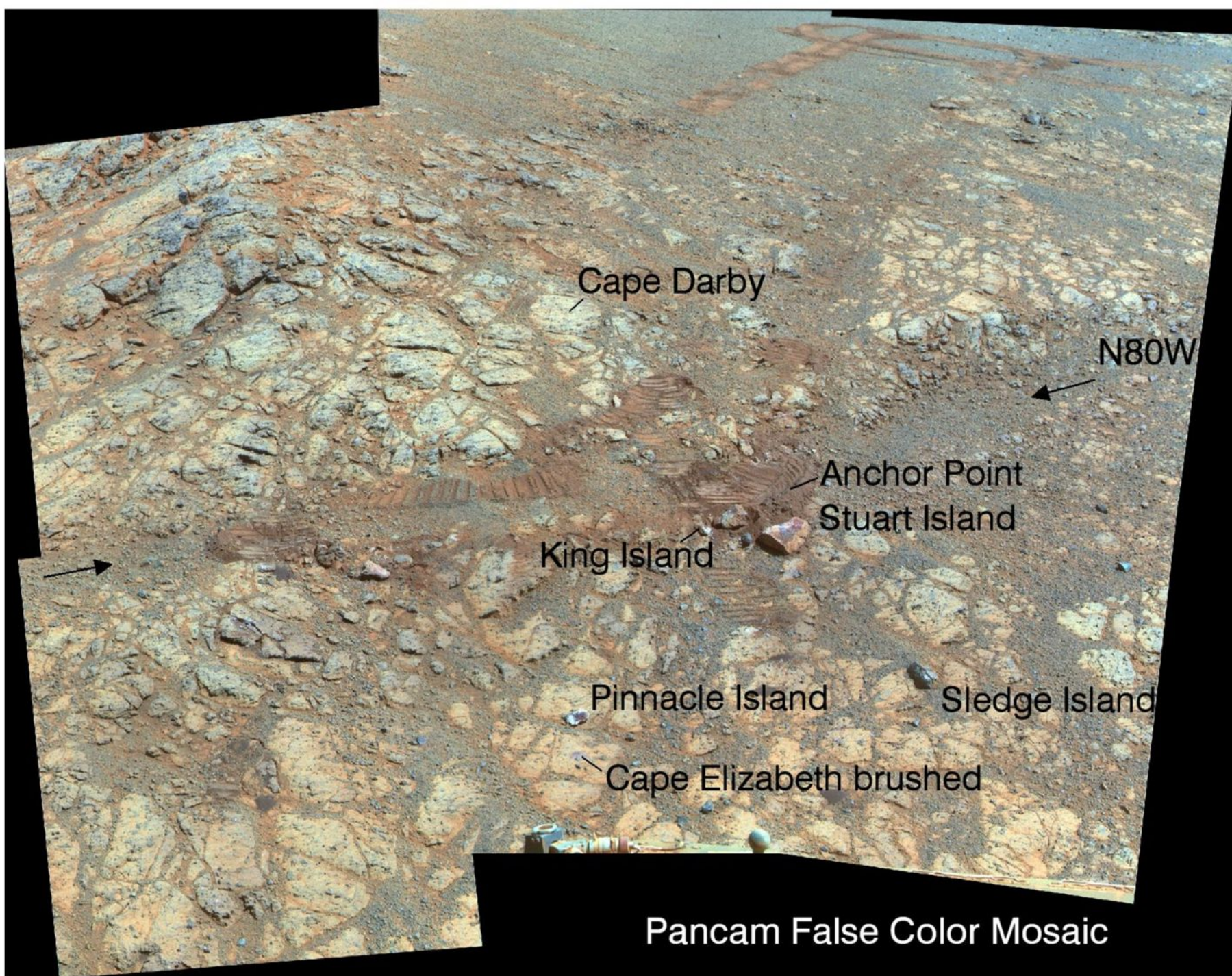
→
N80W

— Cape Elizabeth

— Cape Darby

←
Site 182, pos 194

Rover tracks



Cape Darby

N80W

Anchor Point
Stuart Island

King Island

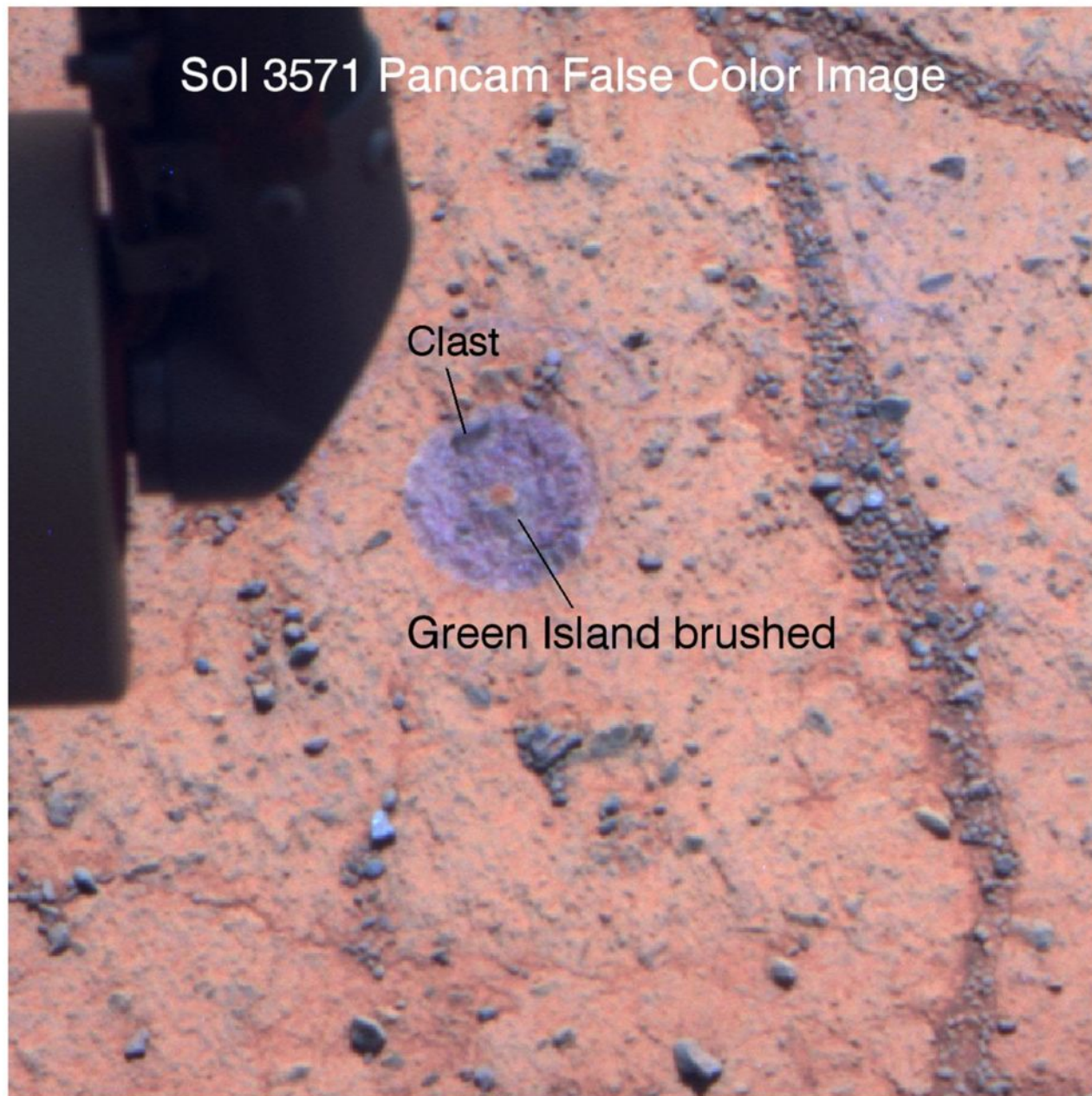
Pinnacle Island

Sledge Island

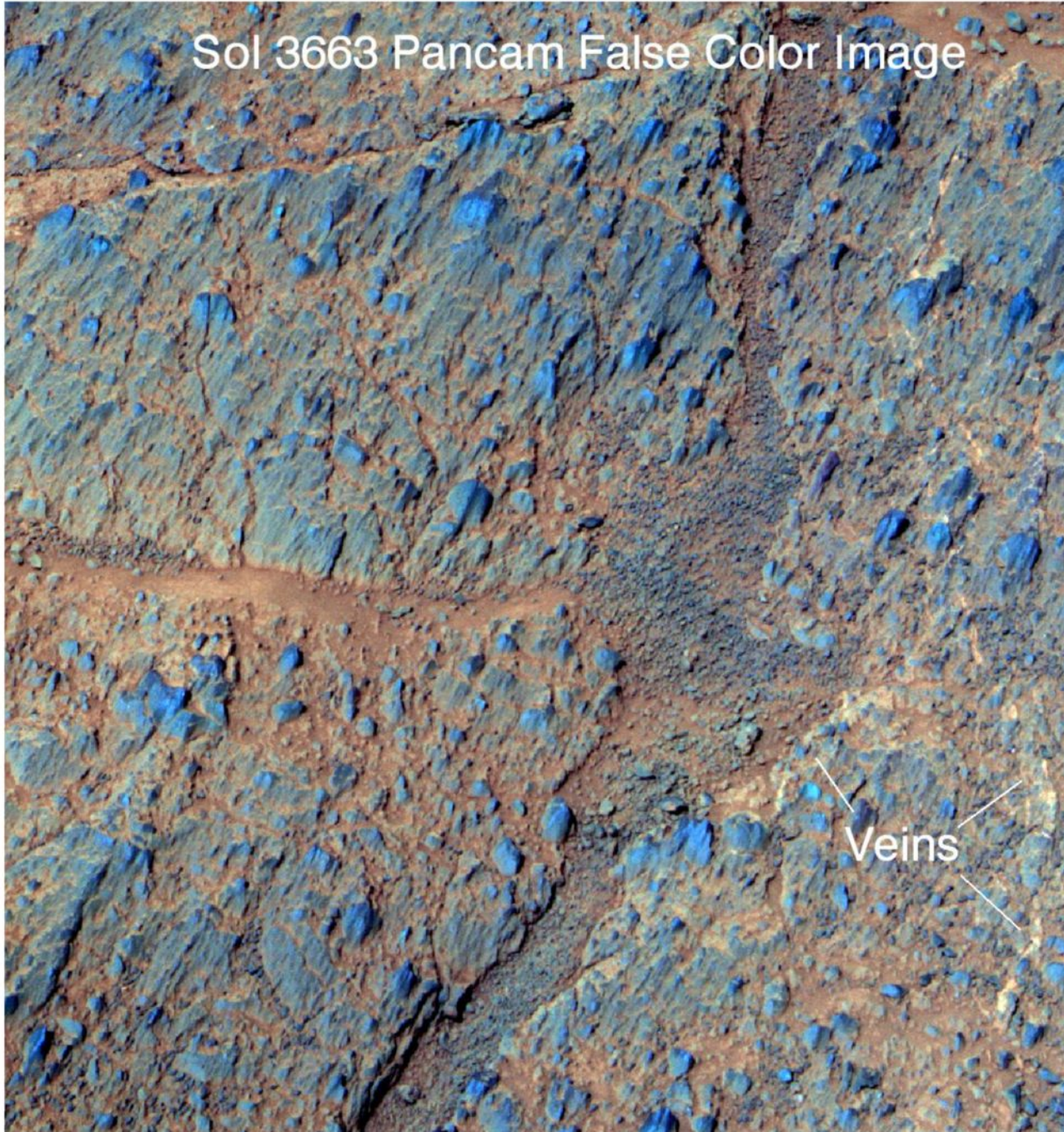
Cape Elizabeth brushed

Pancam False Color Mosaic

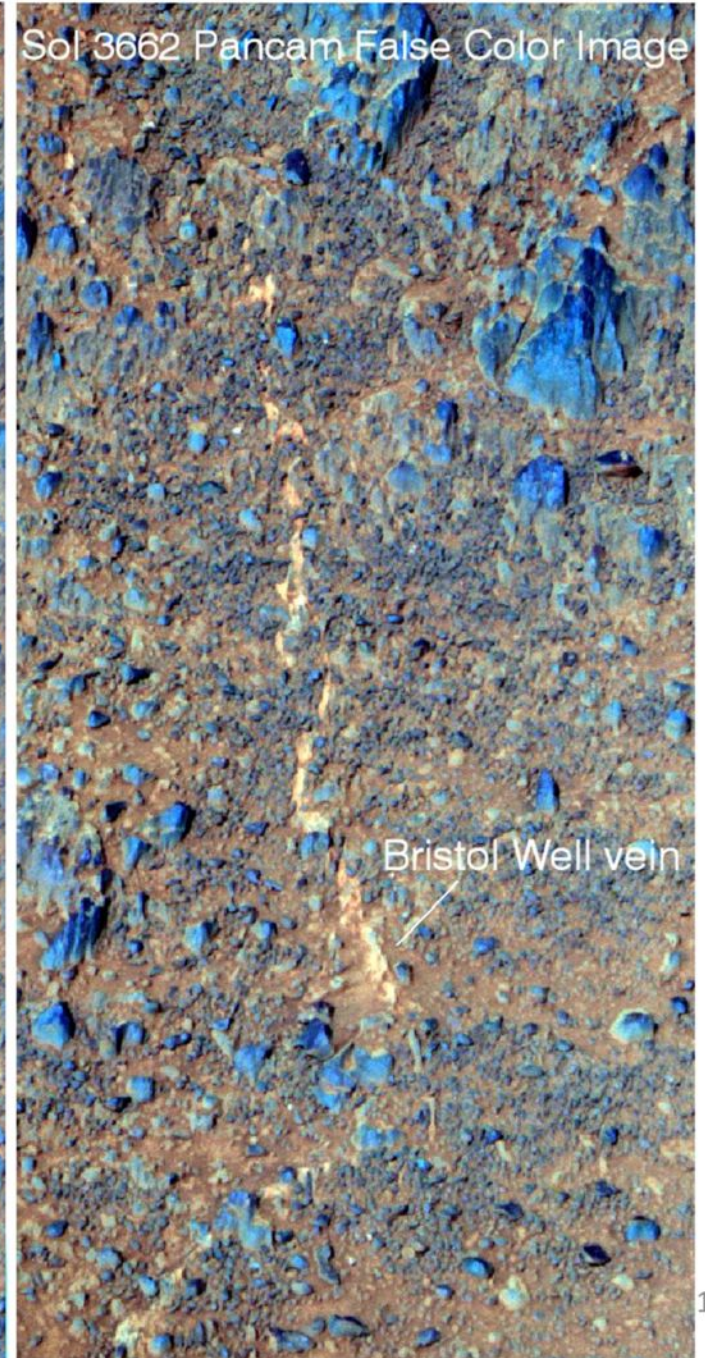
Sol 3571 Pancam False Color Image

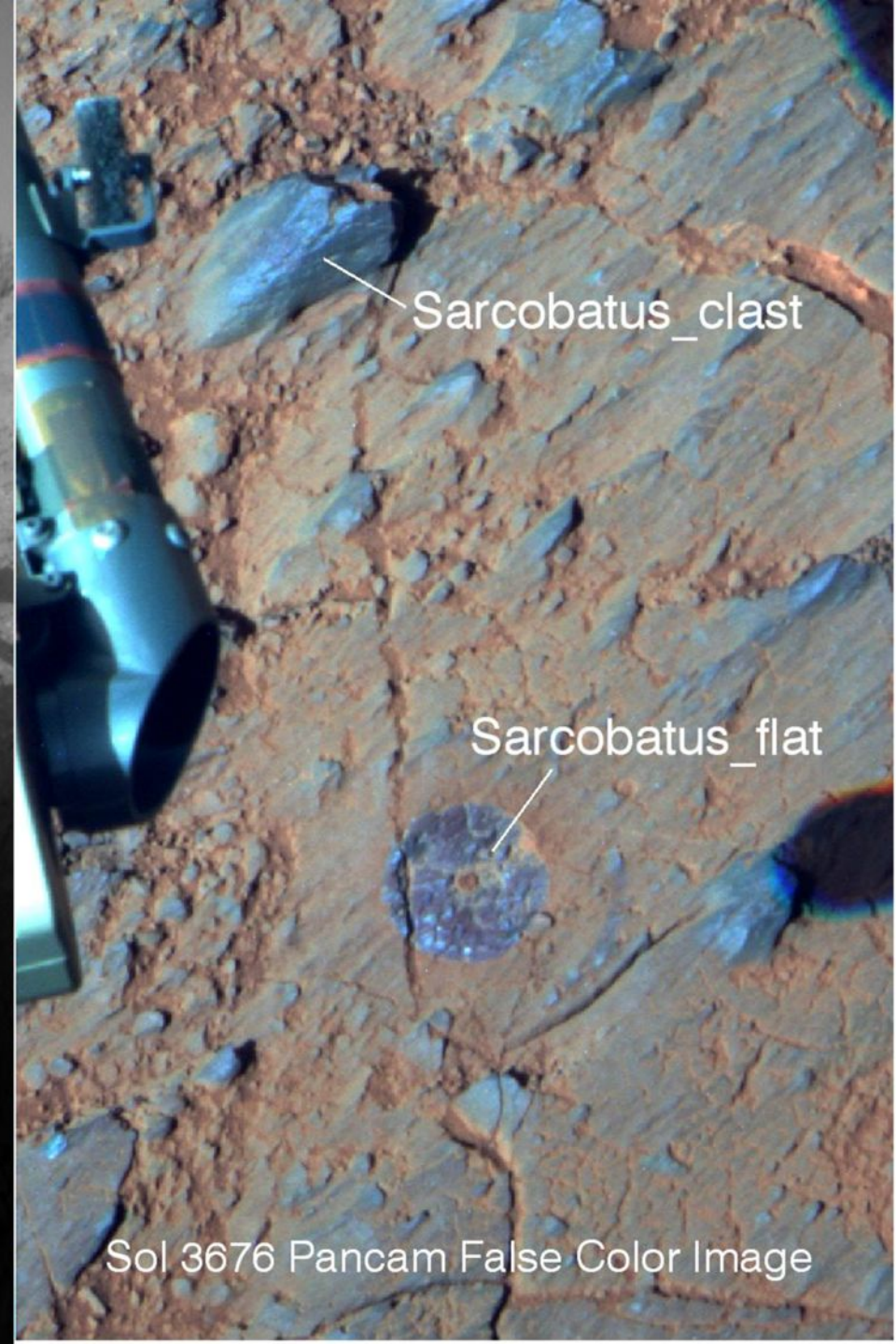


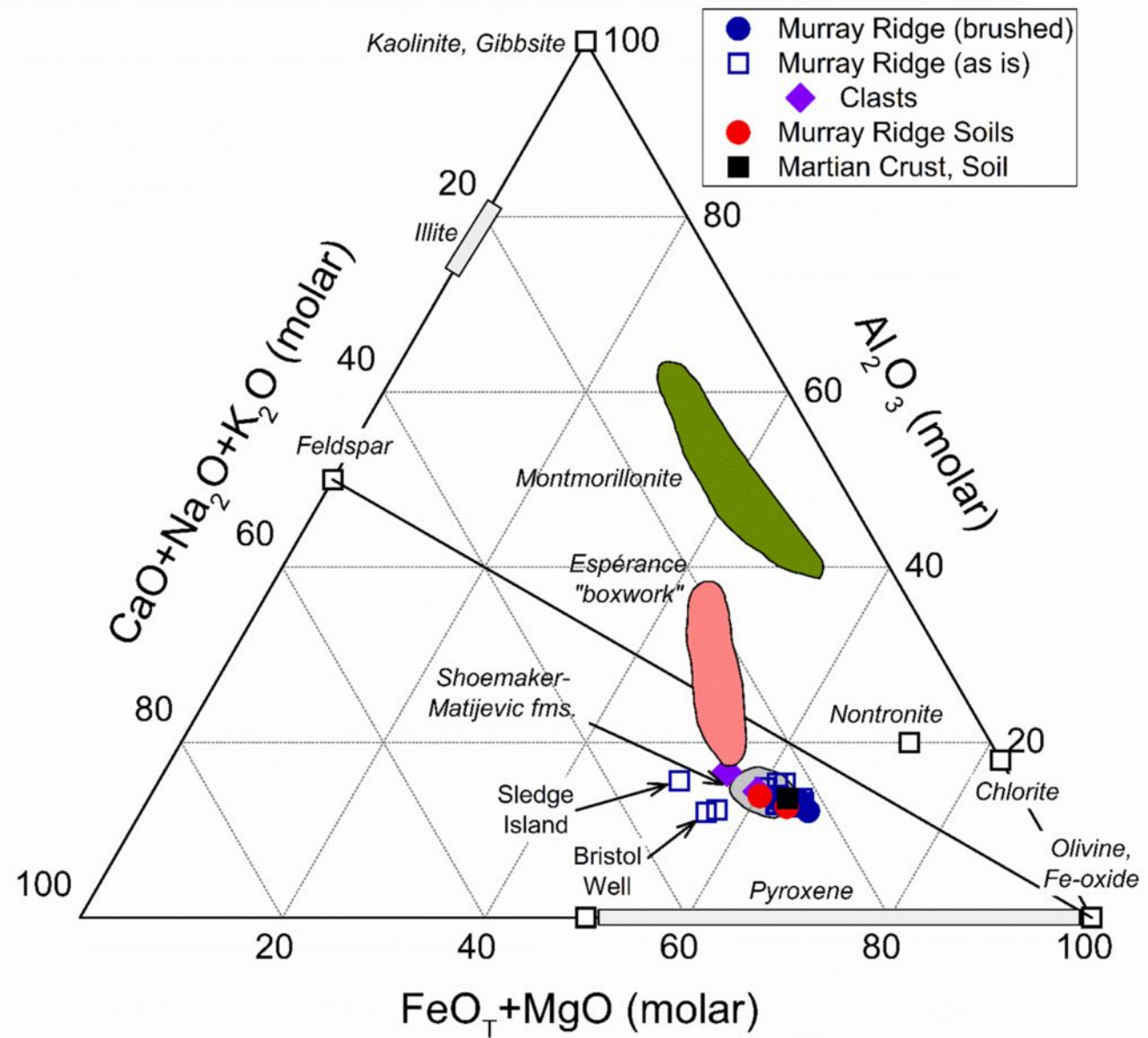
Sol 3663 Pancam False Color Image

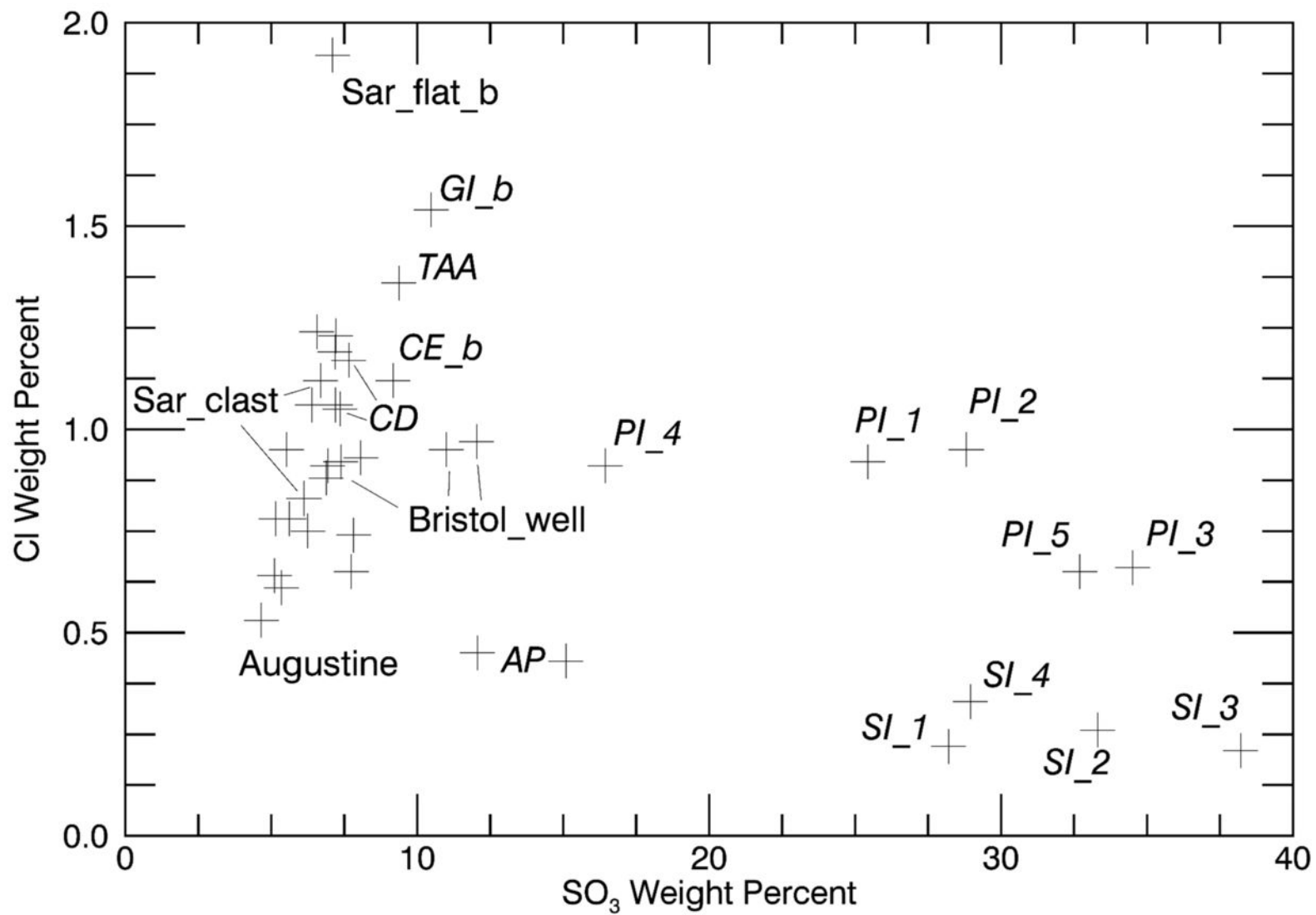


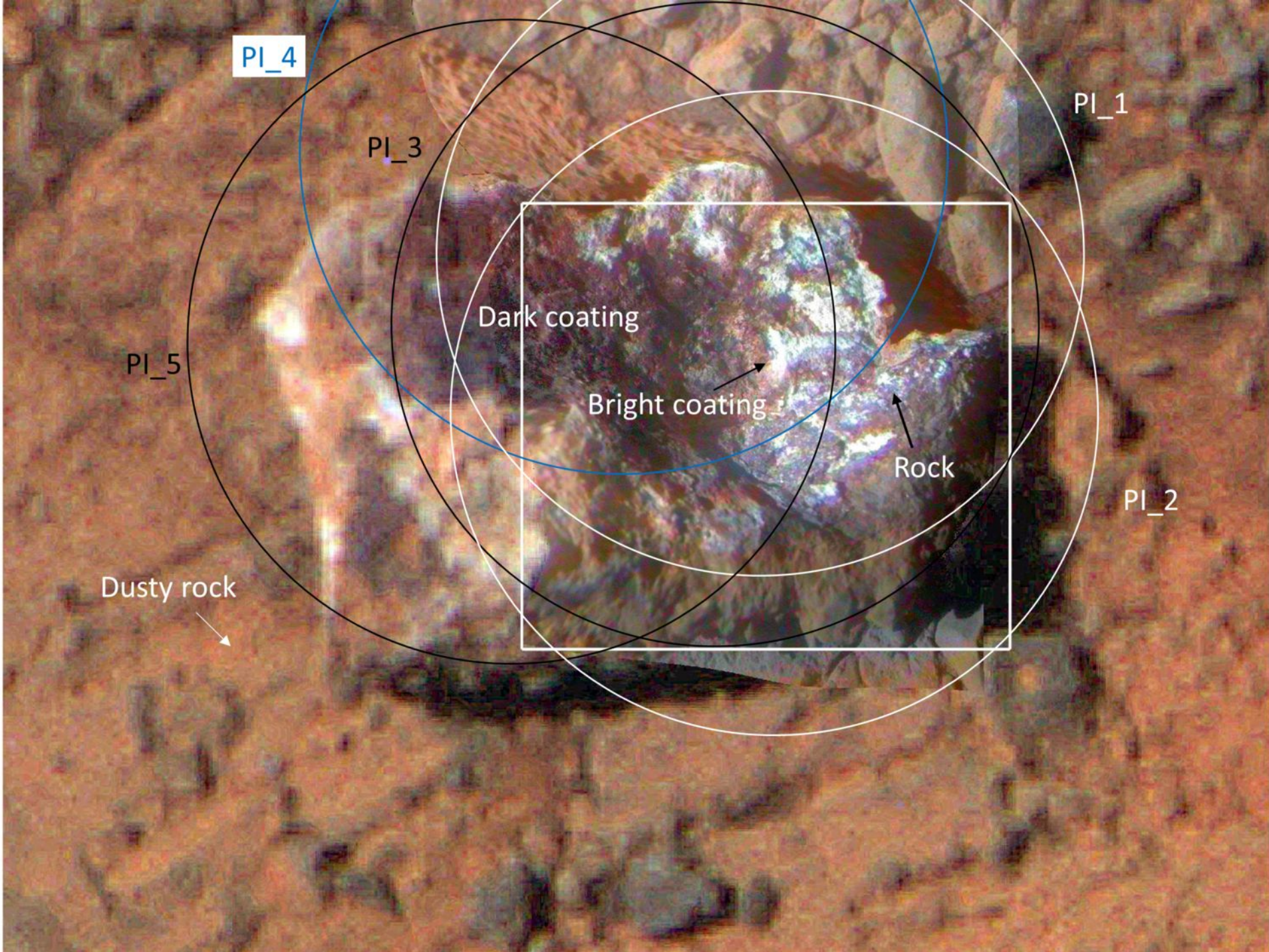
Sol 3662 Pancam False Color Image



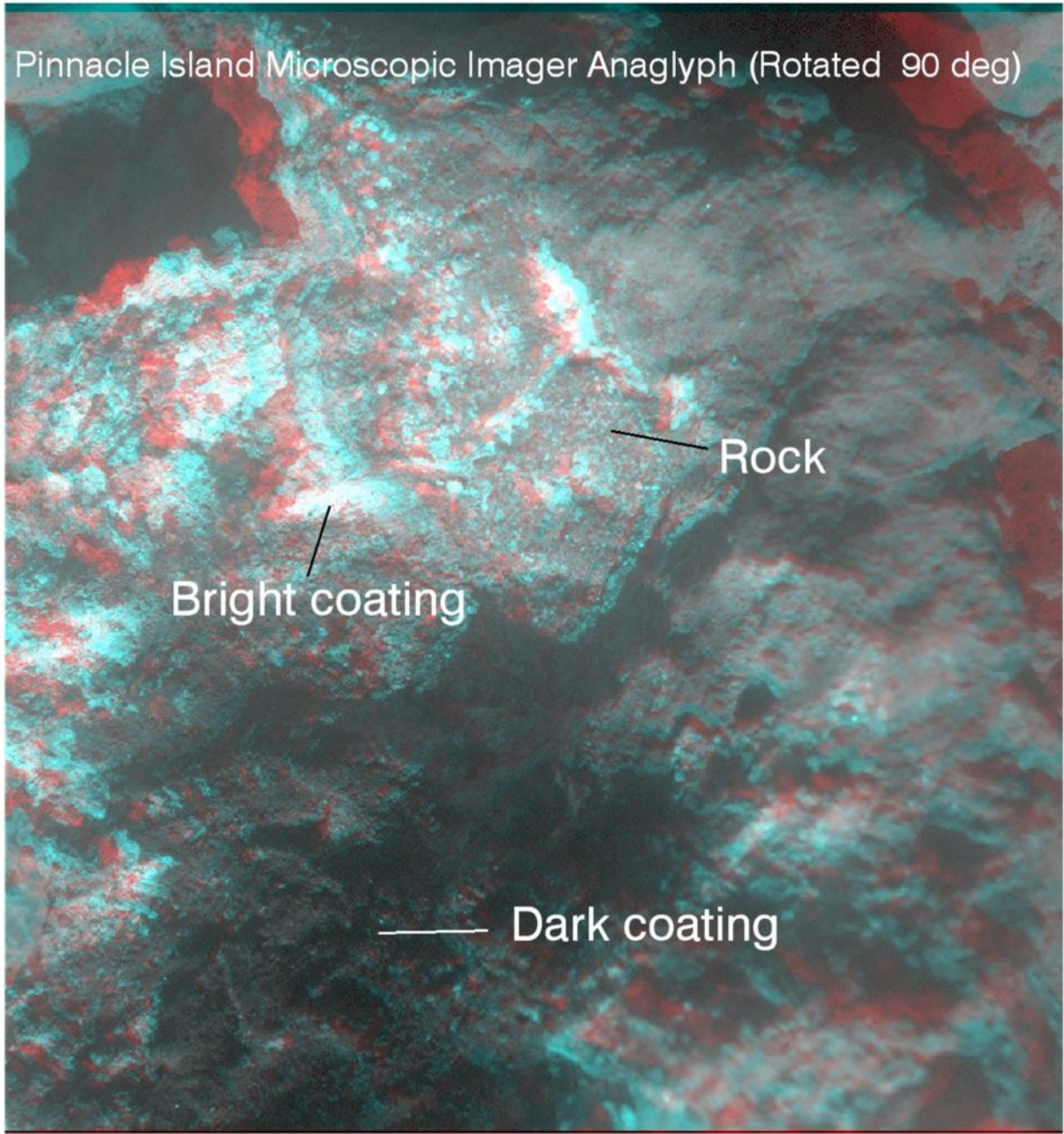






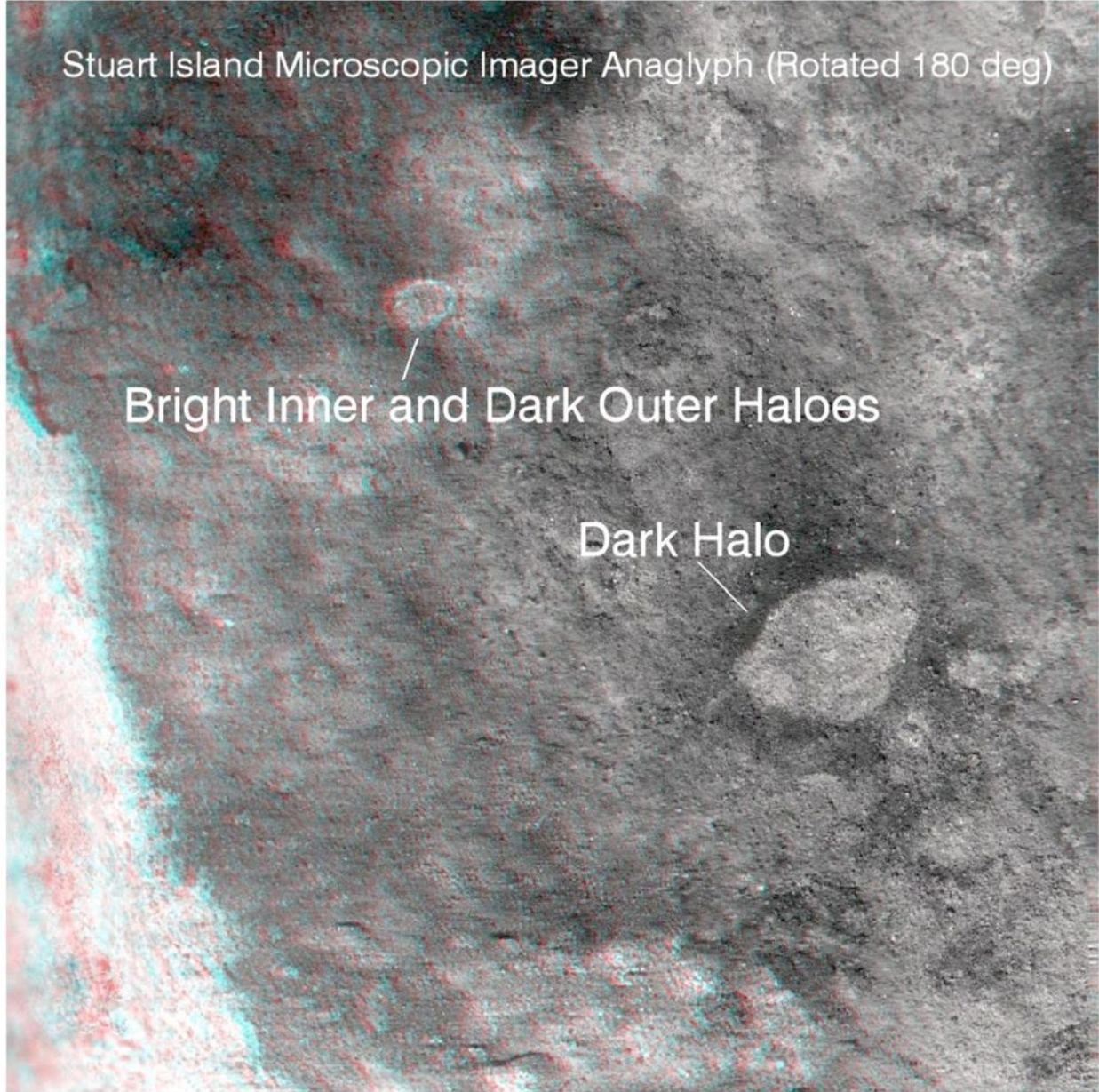


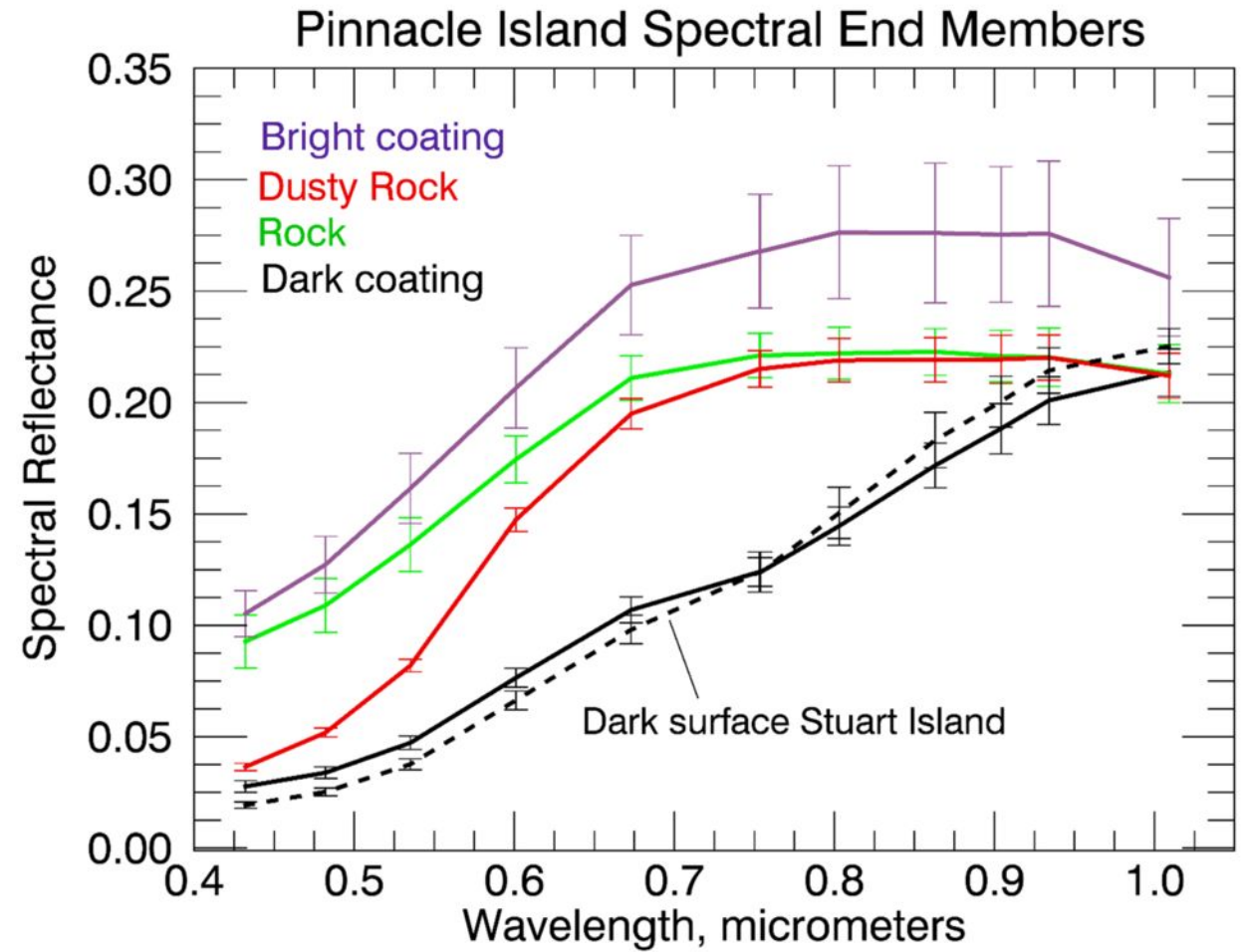
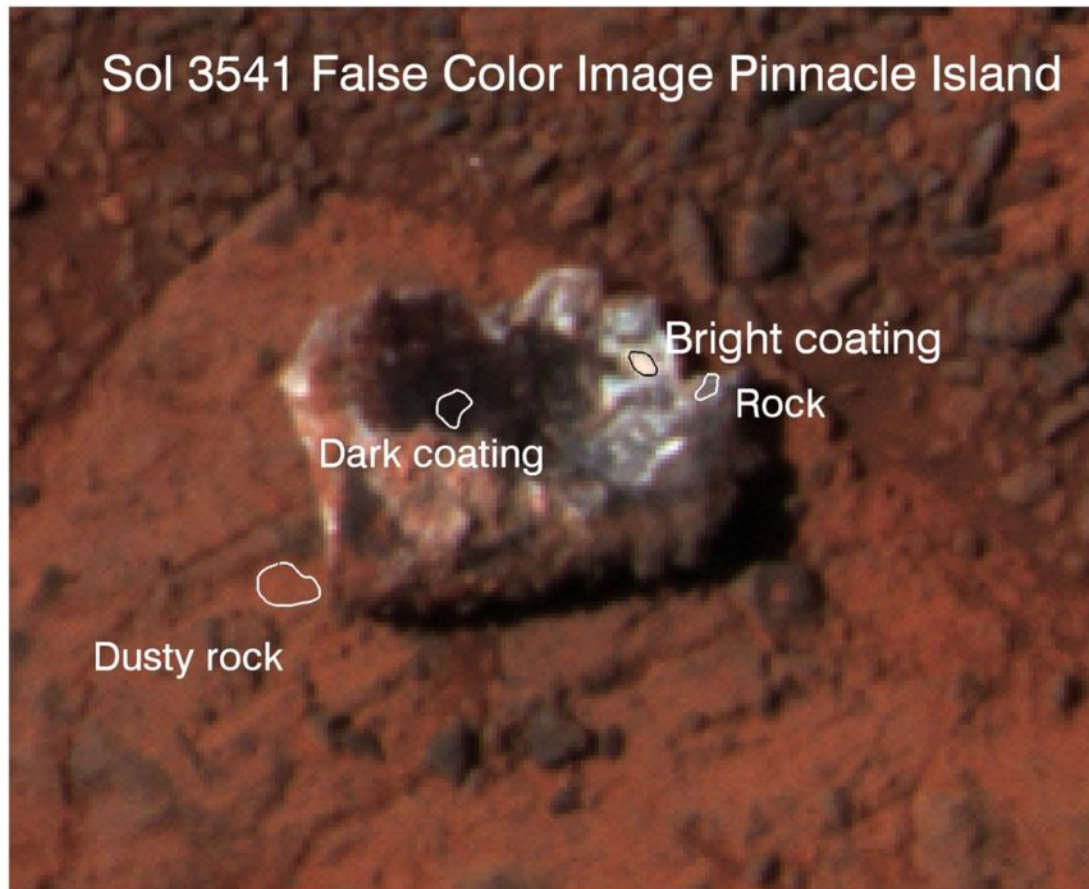
Pinnacle Island Microscopic Imager Anaglyph (Rotated 90 deg)

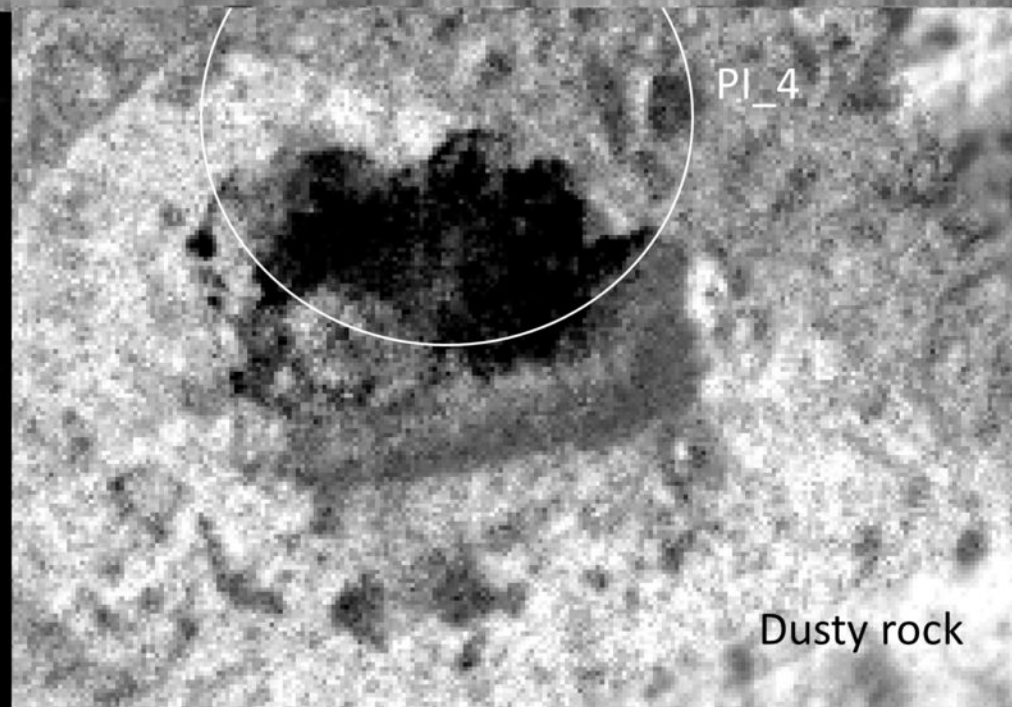
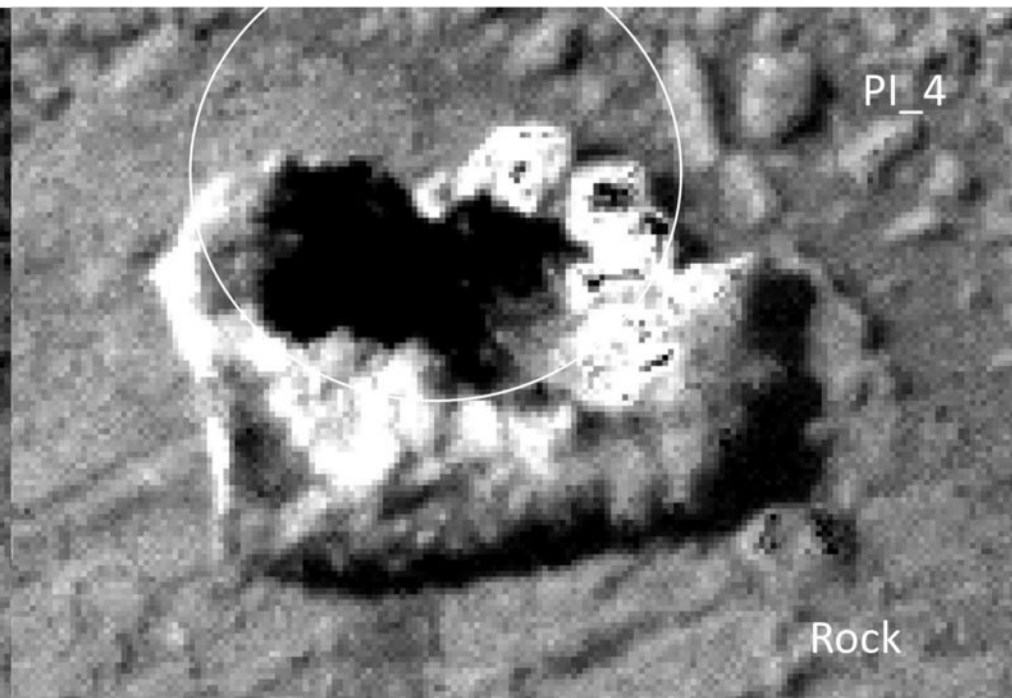
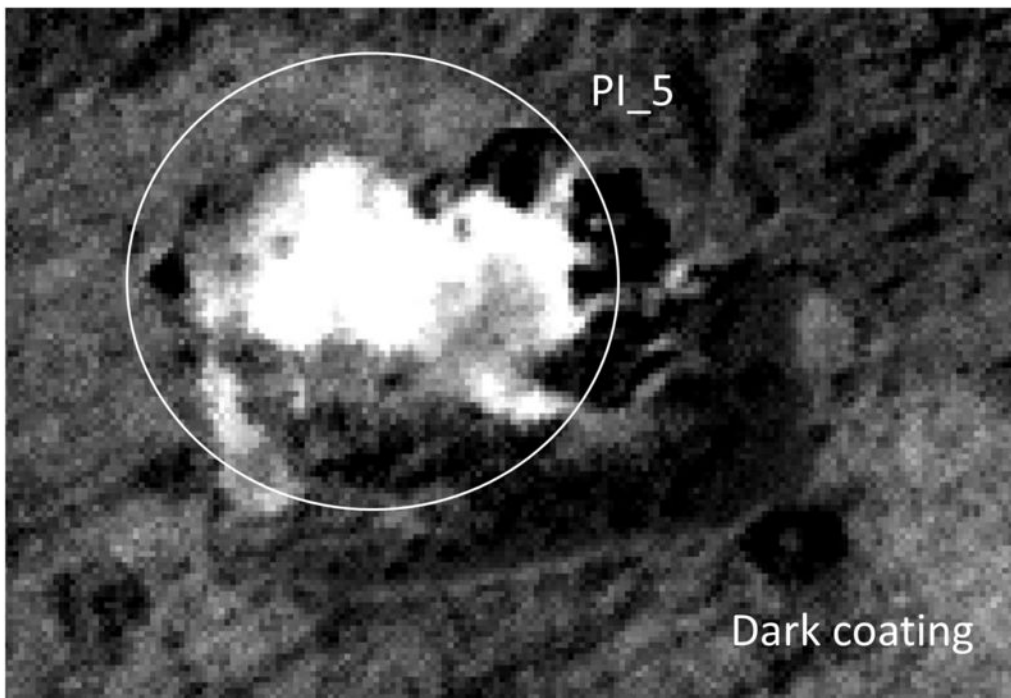


Sol 3576 Pancam False Color Image Stuart Island

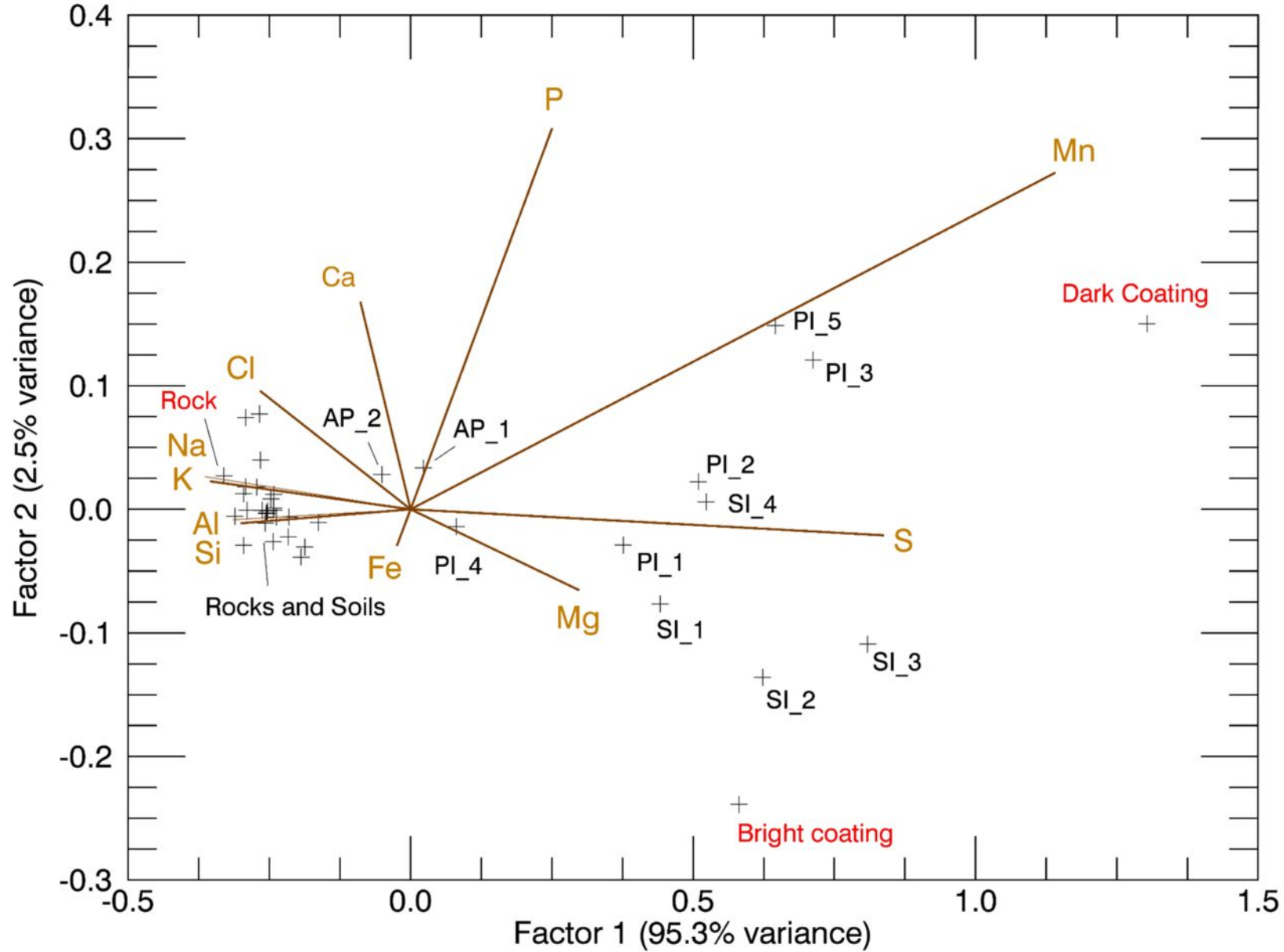


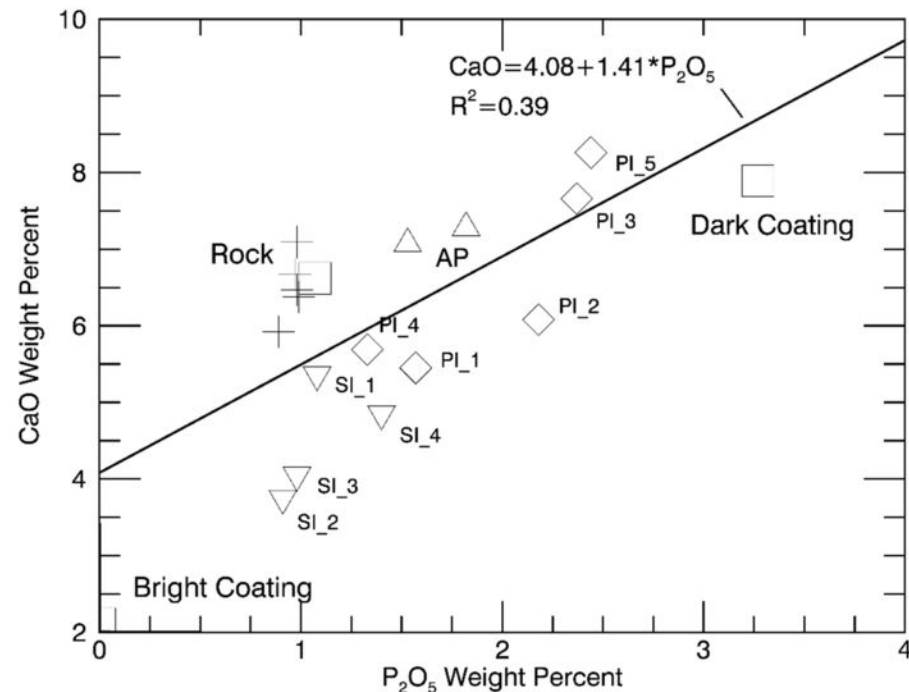
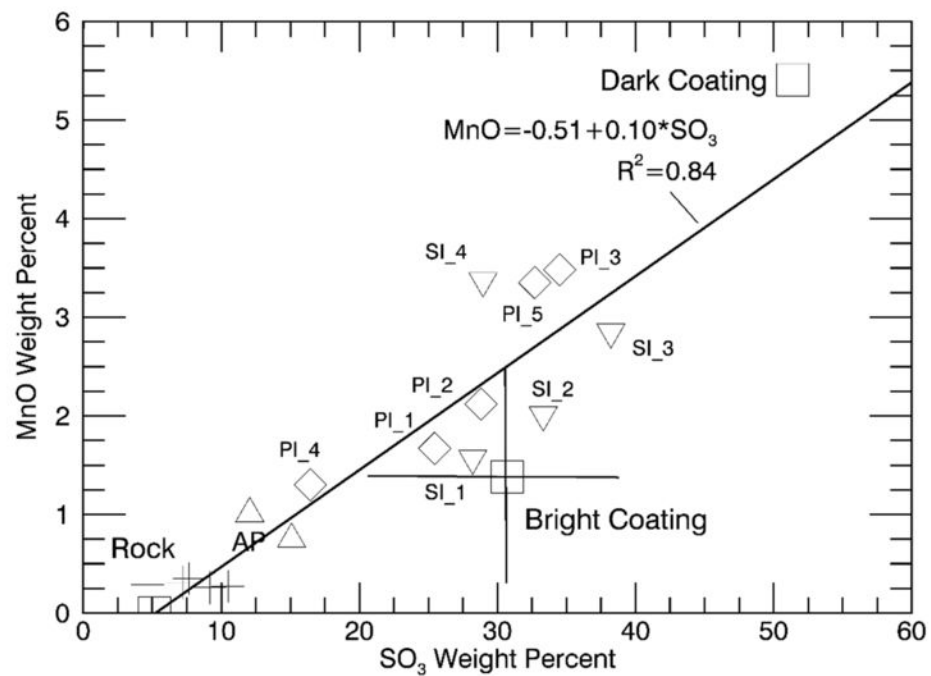
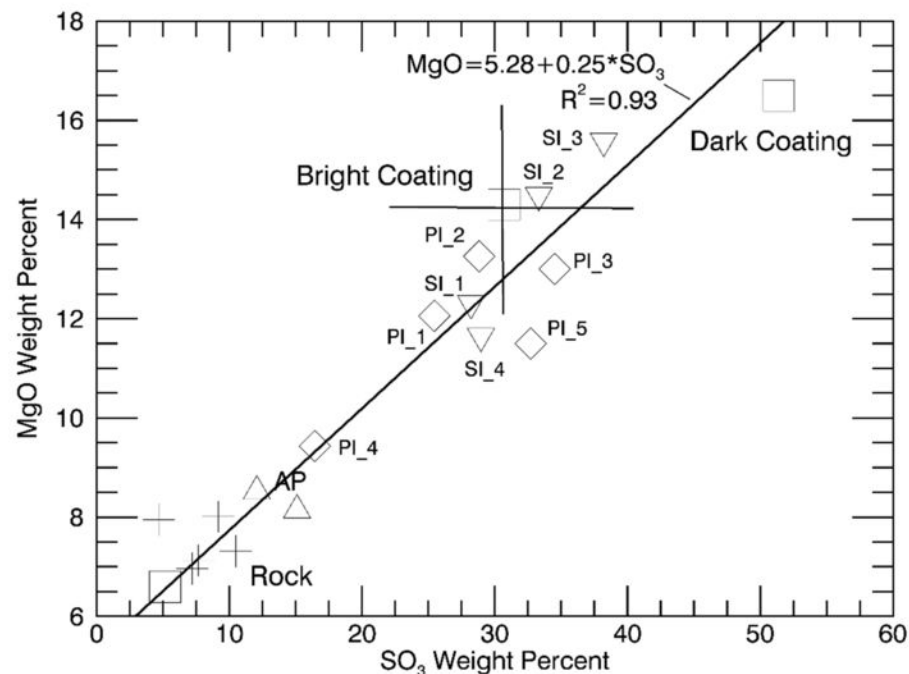
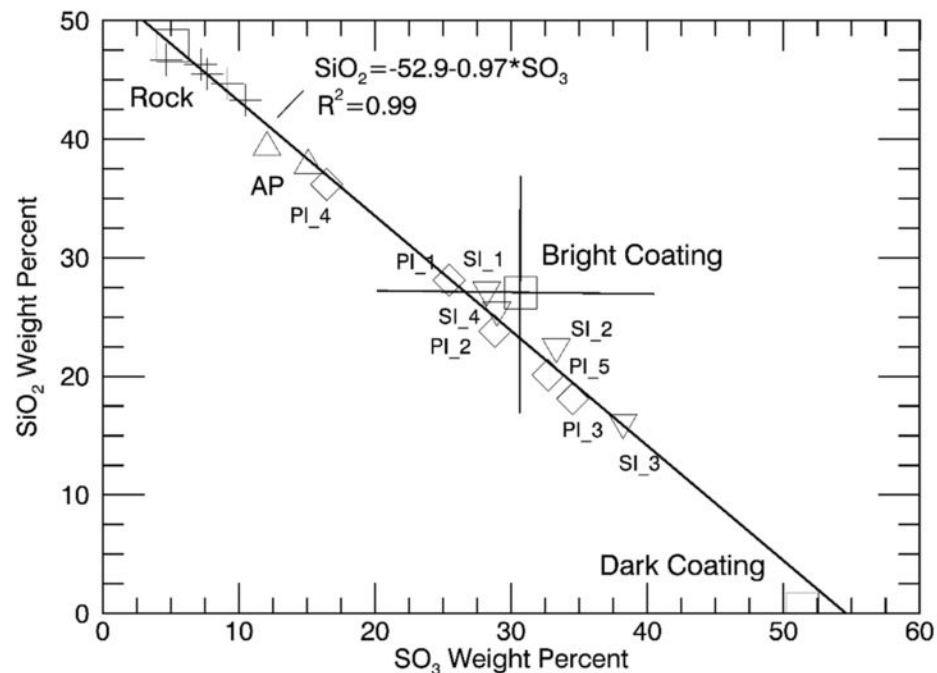


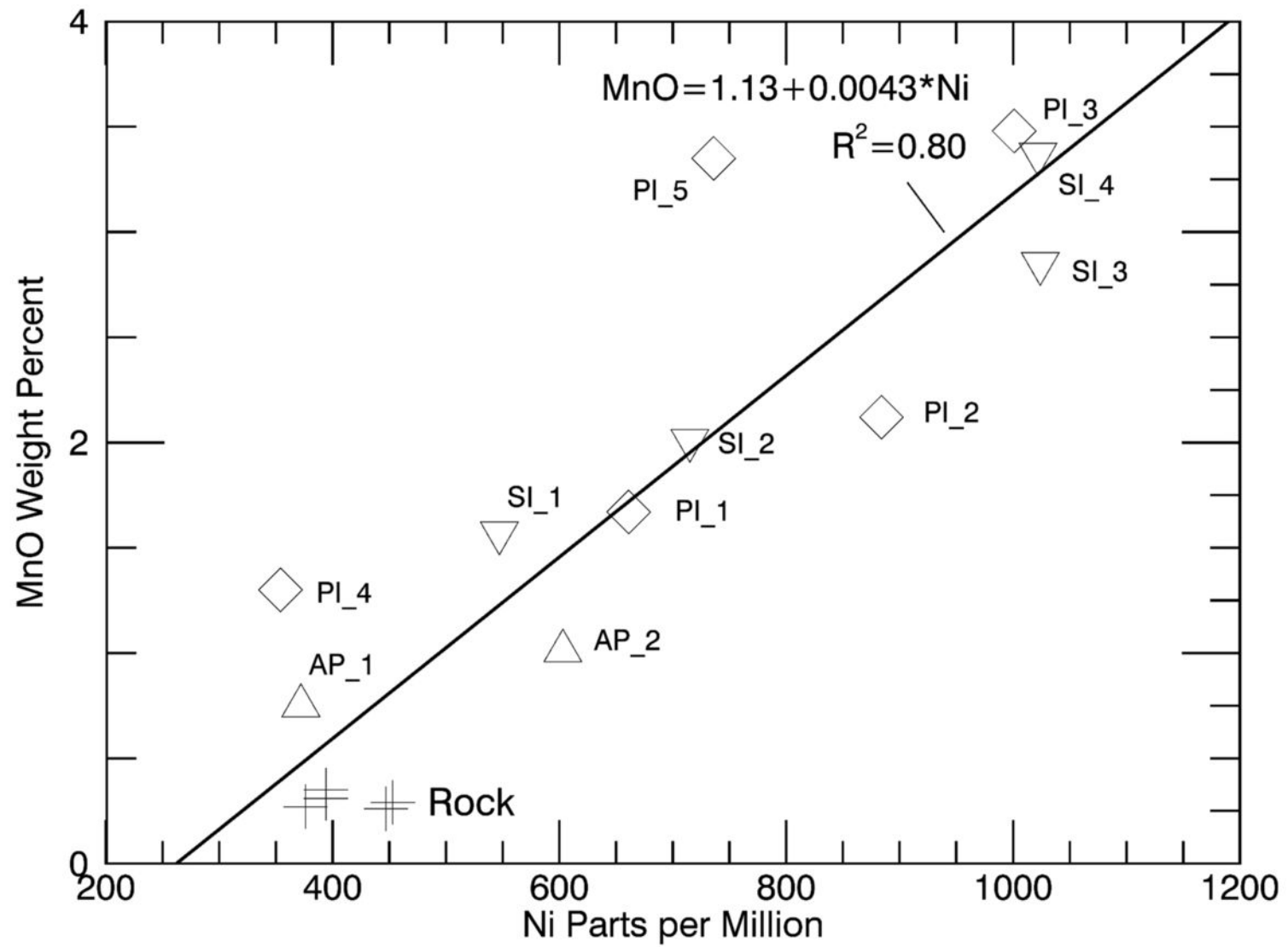


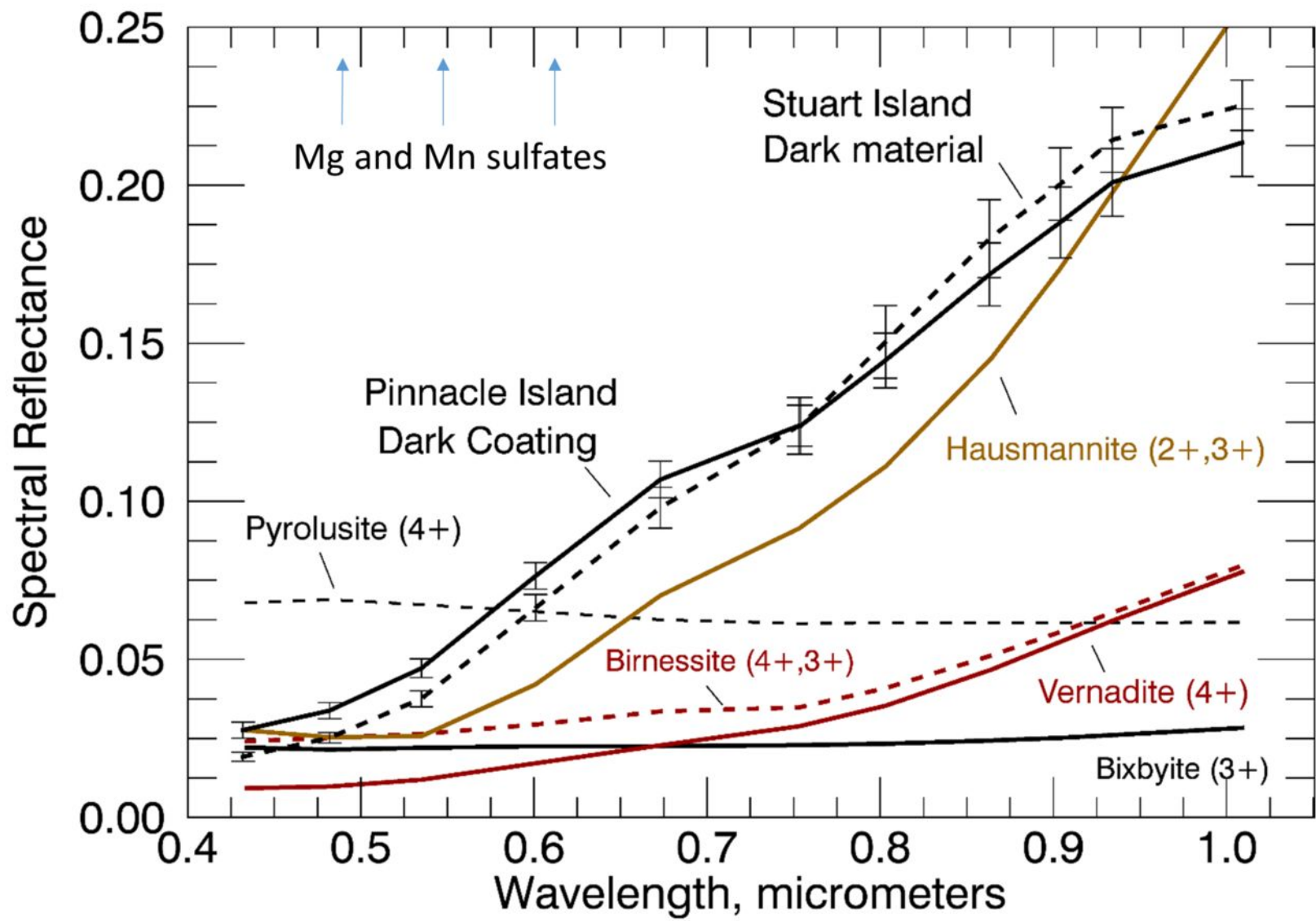


Western Murray Ridge APXS Data (not Bristol Well)

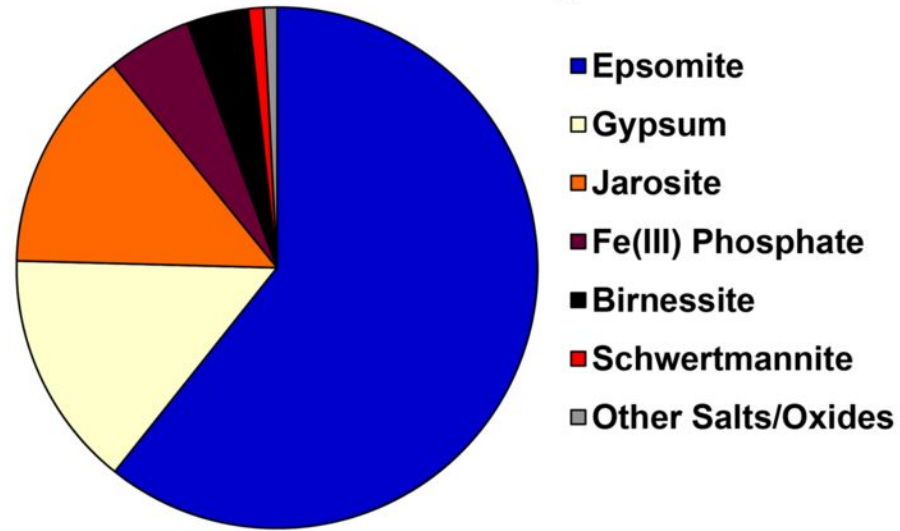








Dark Coating



Bright Coating

